

## Polydopamine-Derived Iron-Doped Hollow Carbon Nanorods as an Efficient Bifunctional Electrocatalyst for Simultaneous Generation of Hydrogen and Electricity

Ajmal Pandikassala, Pranav K. Gangadharan, Radhika Nittoor Veedu, and Sreekumar Kurungot\*



Cite This: *Energy Fuels* 2022, 36, 11245–11260



Read Online

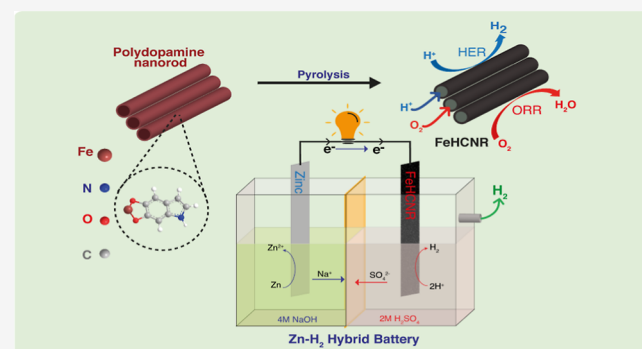
ACCESS |

Metrics & More

Article Recommendations

Supporting Information

**ABSTRACT:** As a step toward developing robust and highly active electrocatalysts for the hydrogen evolution reaction (HER) and oxygen reduction reaction (ORR), we have developed a polydopamine-derived iron-doped hollow carbon nanorod (FeHCNR). It exhibits high electrocatalytic activity toward the HER in acidic media with an overpotential of 29.4 mV at the current density of 50 mA cm<sup>-2</sup>. The catalyst also displays efficient activity for the ORR in acidic media with a high onset potential of 0.97 V. To demonstrate the practical feasibility of the HER characteristics, we designed a new type of Zn–H<sub>2</sub> hybrid battery for the simultaneous generation of hydrogen and electricity by asymmetric electrolysis with the acid catholyte and alkaline anolyte. The system displayed an open-circuit voltage of 1.28 V along with good stability compared to that of the one built using the commercial Pt/C catalyst. This device could generate H<sub>2</sub> gas with a Faradaic efficiency of 97% along with the generation of electricity. Moreover, the outstanding ORR activity of the FeHCNR could be validated by demonstrating an asymmetric-electrolyte Zn–air battery by employing the catalyst as the cathode, which provided an open-circuit voltage of 2.15 V and a power density of 69 mW cm<sup>-2</sup> with the contribution of the electrochemical neutralization energy along with Zn oxidation. Thus, the FeHCNR could perform well toward the HER and ORR during the system-level demonstrations, and this advantage is mainly credited to the hollow nanorod structure of the catalyst, which provides better exposure of the active sites along the outer and inner walls of the system to facilitate the concerned reactions. The open-tube cavity structure of the FeHCNR is supportive for the simultaneous diffusion of the electrolyte and reactants along with more facile dissipation of the products.



### INTRODUCTION

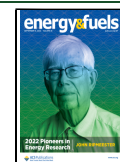
Strict environmental regulations and a growing thrust on the need for a switchover to green energy processes have generated significant attention on the development of efficient hydrogen generation and conversion systems.<sup>1</sup> Even though hydrogen has been considered as one of the most promising and cleanest energy sources to replace conventional fossil-based fuels, commercial-scale production of green hydrogen is still a challenge, and the process needs efficient scientific solutions.<sup>2,3</sup> Among the potential routes available for green hydrogen production, the electrochemical water splitting processes have made significant technological advancements.<sup>4</sup> In a similar way, the electrochemical conversion of hydrogen using polymer electrolyte membrane fuel cells (PEMFCs) is an important process for harvesting the electrical energy from the chemical energy available in hydrogen.<sup>5–8</sup> However, both the electrochemical water splitting process and energy production by PEMFCs need significant improvement with respect to the efficiency and operational cost. Recently, researchers have developed new concepts such as the Li–H<sub>2</sub>O fuel cell,<sup>9</sup> Zn–H<sub>2</sub>O fuel cell,<sup>10</sup> and Al–H<sub>2</sub>O fuel cell,<sup>11</sup> which can

simultaneously generate electricity and produce hydrogen. The alkaline–acid Zn–H<sub>2</sub> hybrid battery is a device similar to the Zn–H<sub>2</sub>O cell in which the neutralization process between the acid and base and the Zn oxidation energy can be concurrently harvested electrochemically.<sup>10,12</sup> The ability of the as-built hybrid battery to produce hydrogen and energy at the same time has been confirmed. Apart from the generation of fuel during the production of electricity, the Zn–H<sub>2</sub> hybrid battery has an additional advantage of utilization of the neutralization energy of water, which causes an increase in the energy density and the voltage output of the system compared to that of the conventional Zn–air batteries (ZABs).<sup>12</sup> Another class of emerging hybrid devices is the asymmetric-electrolyte ZAB (AEZAB), which has the capability to deliver a higher

Received: May 21, 2022

Revised: August 3, 2022

Published: September 1, 2022



performance than that of the conventional ZAB. The additional utilization of neutralization energy makes the AEZAB more fascinating than a typical ZAB in the prospects of future energy generation.

However, demonstrations of such devices have been performed by employing expensive catalysts and separators. Until now, the Pt and Pt-based electrocatalysts have been perceived to be the best for the hydrogen evolution reaction (HER)<sup>13</sup> and oxygen reduction reaction (ORR),<sup>14</sup> which are the important processes involved in the electrochemical production and utilization of hydrogen.<sup>7,8,15,16</sup> However, along with their exorbitant cost, an unsatisfactory durability under the working conditions of the electrochemical systems is a major operational concern. Therefore, exploration into the design of more cost-effective and durable catalysts for these applications is a topic of significant importance at this time.<sup>17</sup> Many activities have been performed for developing potential non-noble metal-based HER and ORR catalysts, including phosphide- and sulfide-based materials.<sup>18</sup> Even though many of these catalysts show better activities for the HER and ORR, they have not yet been able to be considered as credible replacements for the state-of-the-art catalysts.<sup>19</sup> Fe–N species with suitable carbon supports have attracted considerable attention in catalyzing both the HER and ORR.<sup>20–26</sup> Iron-coordinated nitrogen linkage (Fe–N<sub>x</sub>) and particular types of nitrogen species are supposed to be efficient active centers with unique intrinsic activities to facilitate electrochemical adsorption, followed by reduction of the reactants.<sup>20,21</sup> It has been widely proven that along with the composition, the morphology of the substrate also holds a decisive part in determining the overall performance characteristics pertaining to the device-level applications.<sup>27</sup> Considering the compositions of the nitrogen-based heteroatom sites for the HER and ORR, doping of nitrogen is found to be an effective strategy for building the active sites. Charged sites are formed on the carbon sites due to the presence of highly electronegative nitrogen atoms, which profit both the charge transfer and mass transfer during the HER and ORR processes. To further exploit the electrocatalytic activity of the materials, synthetic methods that lead to improved exposure and better accessibility of the active sites are worth studying. In this context, fine-tuning the surface area of the catalysts by hosting hollow structures with anchored active sites along the inner as well as outer surfaces is anticipated to construct more exposed electrochemically active centers along with better feasibility for mass transport than that of the analogous bulk materials.<sup>28</sup> Hence, designing of hollow structured HER–ORR bifunctional electrocatalysts with adequately coordinated Fe–N<sub>x</sub> active sites has been considered to be an interesting approach.<sup>29,30</sup> With this intention, several nitrogen-containing small organic molecules have been extensively applied in the development of N-doped hollow carbon materials.<sup>21,31,32</sup>

Herein, we report the designing of a FeN<sub>x</sub>-based hollow nanorod by utilizing polydopamine (PDA), a kind of melanin-like small organic molecule that contains an enormous number of amine and catechol groups, as a potential bifunctional catalyst for empowering both the HER and ORR. Coordination bonds allow the PDA to attach to metallic ions. In addition to the above advantages, PDA also assists as a decent source of C and N. The homogeneous distribution of the metal nanoparticles and the simultaneous doping of heteroatoms are accredited to these chemical features of PDA. Further, by adopting a unique synthesis process, a hollow structured PDA-

derived carbon nanorod with FeN<sub>x</sub> active centers [iron-doped hollow carbon nanorod (FeHCNR)] could be designed. Thus, the derived FeHCNR catalyst is found to be exhibit decent activity toward both the ORR and HER in acidic conditions with outstanding stability under an electrochemical environment. The open-tube cavity structure and high density of the active sites exposed along the outer and inner walls give the peculiar advantage of improved mass diffusion along with the electrocatalytic activity. This makes the FeHCNR more fascinating toward the electrocatalytic applications that involve gas-phase reactants and products. Additionally, it identifies the practical possibilities and cheaper alternatives for designing energy storage and conversion systems. As a practical means to perceive the hollow morphology of the catalyst at the device level, the performance of the catalyst for the HER has been evaluated by employing the material as the cathode in a new type of Zn–H<sub>2</sub> hybrid battery, which shows an interesting advantage of simultaneous production of electricity and hydrogen fuel. We further verified that the material can serve also as a low-cost ORR catalyst for the AEZAB.

## EXPERIMENTAL SECTION

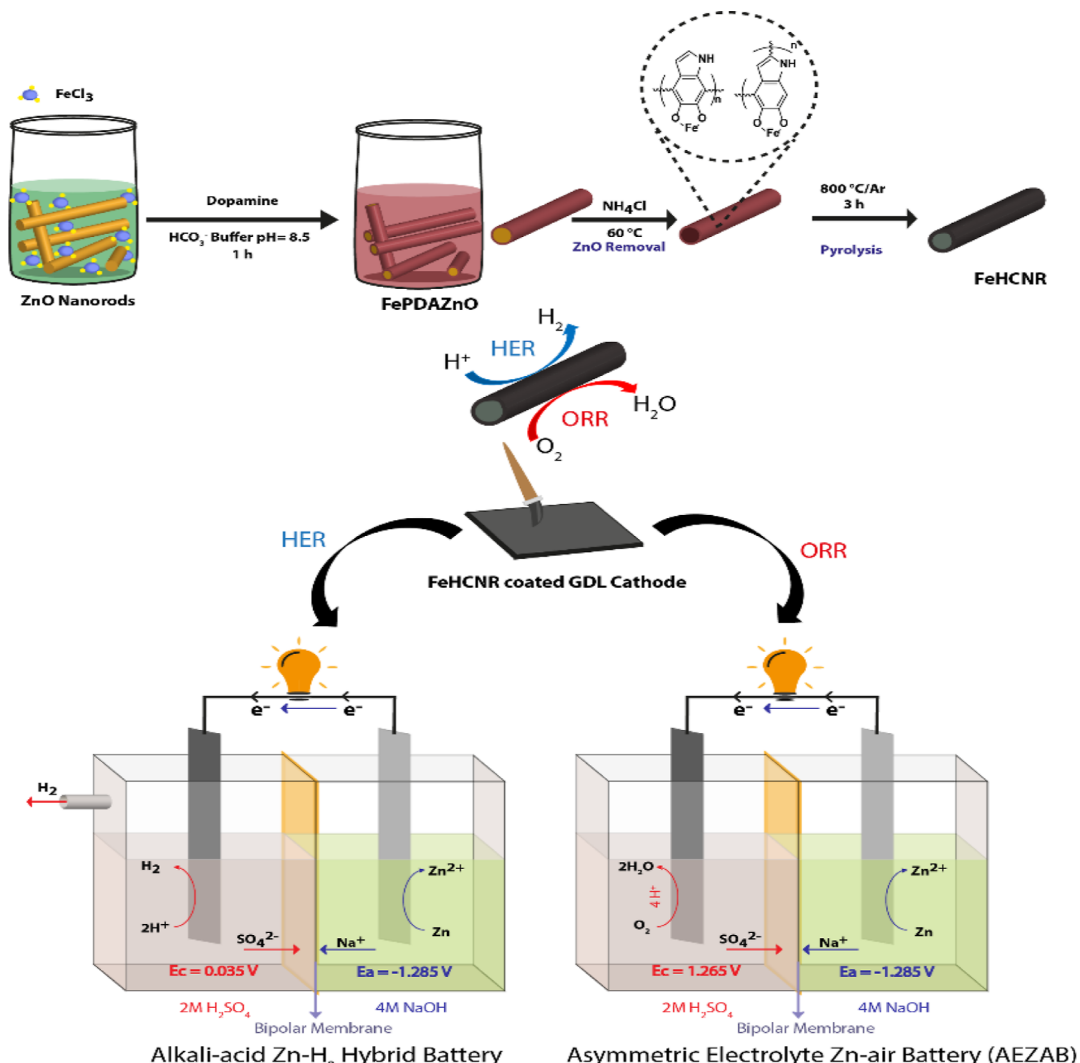
**Reagents.** Chemicals of analytical grade were used as purchased without further purification. Zinc acetate dihydrate [Zn(OAc)<sub>2</sub>·2H<sub>2</sub>O], poly(ethylene glycol) (average molecular weight 400, PEG-400), ethanol (C<sub>2</sub>H<sub>5</sub>OH), sodium hydroxide (NaOH), dopamine hydrochloride (purity 98%), and anhydrous iron(III) chloride (FeCl<sub>3</sub>, 98%) were obtained from Sigma-Aldrich. Sulfuric acid (H<sub>2</sub>SO<sub>4</sub>) was procured from Thomas Baker.

**Preparation of ZnO Nanorods.** The ZnO nanorod was prepared by following a previously reported procedure.<sup>33</sup> In a typical process, about 1.15 g of Zn(OAc)<sub>2</sub>·2H<sub>2</sub>O, 7.5 ml of PEG-40, and 3.0 g of NaOH were mixed in 30 ml of ethanol and subjected to ultrasonication for about 30 min at room temperature. Subsequently, in a 50 mL Teflon-lined stainless-steel autoclave, the above mixture was kept for 12 h at 120 °C. The resulting product underwent five rounds of washing with distilled water and ethanol. The white powder obtained was then dried in a vacuum oven at 60 °C for future use.

**Preparation of the FeHCNR.** For preparing the FeHCNR, about 20 mg of already synthesized ZnO nanorod and 1 mM FeCl<sub>3</sub> were dissolved in 10 mL of bicarbonate buffer (pH of 8.5) solution containing 10 mg of dopamine hydrochloride. Then, the solution was stirred at room temperature for 60 min. As the pH-induced oxidation progressed, the color of the solution gradually turned dark brown and the dopamine was self-polymerized over the ZnO to form PDA-covered ZnO nanorods (FePDAZnO). Thus, the obtained FePDAZnO was separated by centrifugation before being rinsed with deionized water. The obtained product was then vacuum-dried at ambient temperature. To etch out the ZnO template, FePDAZnO was added into a 2 M aqueous solution of NH<sub>4</sub>Cl, and the suspension was stirred for 20 min at 60 °C. Lastly, the ZnO-free iron-doped PDA nanorods were attained by centrifugation, washing with deionized water, and drying using a vacuum oven at 60 °C. The material was subsequently annealed at 800 °C under an Ar atmosphere for 2 h, followed by the treatment with 0.5 M H<sub>2</sub>SO<sub>4</sub> at 60 °C to eliminate the non-reactive and unstable residues. Thus, the obtained material after being washed three times with water and dried is designated as the FeHCNR. Also, for the comparative study, a control sample without a hollow structure has been prepared by directly annealing FePDAZnO at 800 °C under an Ar atmosphere for 2 h, and the obtained sample is named as FePDCZnO. Whereas the FeHCNR has a hollow tubular morphology with the well-coordinated Fe–C–N type active sites exposed along the inner and outer walls of the rods, the ZnO core present in FePDCZnO lacks the hollow nature and its active sites are exposed only along the outer surface.

**Hybrid Battery Fabrication.** For the hybrid batteries, the cathode was prepared by applying the catalyst slurry using a brush

**Scheme 1.** Schematic Illustration of the Preparation of the FeHCNR Electrocatalyst and Its System-Level Demonstrations for the Zn–H<sub>2</sub> Hybrid Battery and AEZAB



on the carbon gas diffusion layer (GDL) with an active area of 1 cm<sup>2</sup>. The catalyst ink was formed by subjecting the FeHCNR to an ultrasonic bath along with 20 wt % of the Nafion ionomer in an IPA solvent for 1 h. The ionomer (Nafion) to carbon ratio was fixed as 0.40 for the electrode fabrication with a catalyst loading of 1.0 mg cm<sup>-2</sup>. To get the solvents off the brush-coated electrode, it was dried at 120 °C in a vacuum oven for 6 h. A Zn foil of an active area of 1.0 cm<sup>2</sup> having a 0.20 mm thickness was taken as the anode. Both the electrodes were kept in a H-type glass cell containing a volume of 50 ml in each compartment. A commercial Zn foil anode was dipped in a 4 M NaOH anolyte, and the FeHCNR cathode was immersed in a catholyte chamber filled with 2 M H<sub>2</sub>SO<sub>4</sub> as the catholyte. A bipolar membrane (BPM) was used to separate both the chambers. For the Zn–H<sub>2</sub> hybrid battery operation, the catholyte was saturated with N<sub>2</sub> gas. However, the O<sub>2</sub> gas was continuously purged in the cathode chamber during the functioning of the asymmetric ZAB.

**Characterization.** Morphological features were investigated by scanning electron microscopy (SEM) using a scanning electron microscope (Quanta 200 3D FEI instrument) and transmission electron microscopy (TEM) using the FEI Technai G2 T20 instrument, which was operated at 200 keV. Powder X-ray diffraction (XRD) profiles were recorded to check the crystallinity with the help of a PANalytical X'Pert Pro instrument using Cu K $\alpha$  (1.5418 Å) radiation with a scan rate of 5° min<sup>-1</sup>. Thermogravimetric analysis (TGA) was performed at a heating rate of 10 °C min<sup>-1</sup> under an O<sub>2</sub>

atmosphere from 25 to 900 °C to determine the metal loading over the carbon using an STD Q600 DSC-TGA thermogravimetric instrument. The Raman spectra were recorded on an HR 800 RAMAN spectrometer (Jobin Yvon, Horiba, France) equipped with a 632.1 nm red laser. A SPECTRO ARCOS Germany, FHS 12 instrument was used for the inductively coupled plasma optical emission spectrometry (ICP-OES) analysis. Using a VG Microtech Multilab ESCA 3000 spectrometer, X-ray photon emission spectroscopy (XPS) analysis of the samples was performed. The specific surface area, pore size distribution, and pore volume were studied by utilizing a Quantachrome Quadrasorb automatic volumetric instrument at a temperature of 77 K. The Brunauer–Emmett–Teller (BET) surface area was determined by multipoint BET analysis, and the average pore diameter was calculated by the nonlocal density functional theory (NLDFT). Electrochemical characterizations were performed by using the Pine Research Instrument's rotating disk electrode (RDE) and rotating ring disk electrode (RRDE) setup connected to a BioLogic VMP-3 PG Stat.

## RESULTS AND DISCUSSION

The preparation of the FeHCNR is illustrated in Scheme 1. The zinc oxide nanorods (ZnONRs) synthesized by a solvothermal method reported previously<sup>33</sup> were used as the template for the preparation of the hollow carbon nanorods.

The dopamine was self-polymerized over the surface of the obtained ZnONR template under a weak alkaline condition with an iron precursor to form iron-coordinated PDA nanorods (FePDAZnO). The slow polymerization ensures the complete coverage of the PDA layer over the ZnONR template, leading to the formation of a bilayer structure. Further, the iron-incorporated hollow PDA nanorod architecture was attained by the removal of the ZnONR template. The 2 M NH<sub>4</sub>Cl used for the removal of the template selectively reacts with the Zn and etches away ZnO by leaving the outer layer intact. The etching of the ZnO nanorod template holds a significant part in the development of the hollow structure of the FeHCNR. The amphoteric nature of ZnO helps it dissolve in either basic or acidic solutions. Since PDA contains a huge number of basic amino groups, it is not a decent acid-resistant substance. In contrast, it can be dissolved in a basic solution. Therefore, to maintain the morphology of PDA as such, it is essential to follow a new approach to etch out the ZnO template in a solution with neutral pH. The experimental results show that 2 M NH<sub>4</sub>Cl aqueous solution with a usual pH of 4.5 is a perfect etching agent for Zn. Subsequent high-temperature annealing of the hollow PDA shell coordinated with Fe<sup>3+</sup> ions transform the matrix into the FeHCNRs enriched with the FeN<sub>x</sub> active sites. During the course of the high-temperature annealing, the PDA gets converted into graphitic carbon, which has nitrogen and iron coordination in its matrix, respectively, generated from the amino group of the dopamine and the iron precursor. The graphitization helps the material achieve electrical conductivity, which is important for ensuring the electrocatalytic functioning of the system **Figure 1a,b** show the field emission SEM (FESEM) and TEM images of FePDAZnO, respectively. The bilayer structure of FePDAZnO has a rod-like morphology since it is formed from the ZnONR template. The thin layer coating of the PDA layer differentiates FePDAZnO from the ZnONR. The FESEM and TEM images of ZnO given in **Figure S1** depict the rod-like morphology of the template material. The average length and diameter of the ZnO nanorods are found to be between 150–250 and 20–40 nm, respectively, from the histogram tabulated using more than 60 nanorods in the TEM image. The particle size histogram of the ZnONR is shown in **Figure S2**. However, FePDAZnO has an extra layer of PDA coating, which has a thickness of around 16 nm (**Figure 1b**). Further, the FESEM images of the FeHCNR with different magnifications, as shown in **Figure 1c,d**, illustrate the retention of the rod-like morphology of the parent sample (i.e., FePDCZnO) even after the high-temperature annealing. In the TEM images presented in **Figure 1e,f**, the hollow nature is clearly visible. The inner diameter of the rods in the FeHCNR is about 17 nm, with the length ranging from 100 to 500 nm, while maintaining the wall thickness of about 13 nm. It should be noted that subsequent to the high-temperature annealing, the diameter of the nanorod gets reduced to half from 40 nm to about 17 nm due to the thermal stress exerted on the material during the annealing process. The TEM image of the FeHCNR does not reveal the presence of any trapped particles originating from the iron moiety. In **Figure S3**, the energy-dispersive X-ray spectroscopy mapping of the FeHCNR confirms that the elements C, N, and Fe are distributed uniformly on the hollow carbon structure. The removal of ZnO nanorods by NH<sub>4</sub>Cl is found to decrease the uniformity of the tubular morphology to a certain extent.

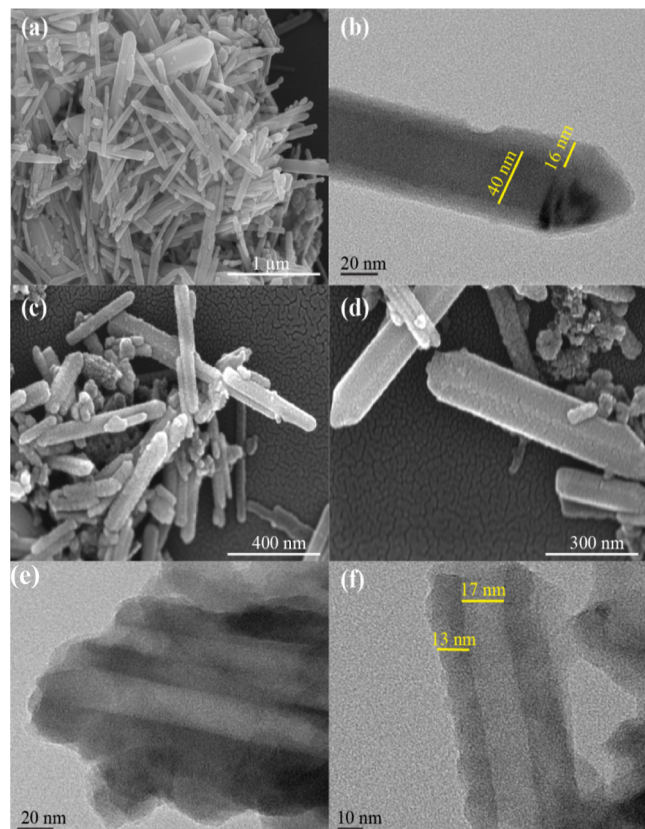


**Figure 1.** (a) FESEM and (b) TEM images of FePDAZnO, (c,d) FESEM images of the FeHCNR with different magnifications, and (e,f) TEM images of the FeHCNR with different magnifications.

XRD analysis has been performed to find out the crystal phase characteristics of the FeHCNR. The comparative XRD profiles of the ZnO nanorod and FeHCNR are presented in **Figure 2a**. The graphitic carbon's (002) plane of the FeHCNR can be assigned to the broad peak that appeared at 23.1°.<sup>34</sup> This points toward the attainment of the graphitic carbon phase from the parent hollow PDA nanorods due to the high-temperature annealing at 800 °C. All the remaining sharp diffraction peaks from 30 to 70° present in the FeHCNR are in good agreement with the signature peaks corresponding to the different phases of Fe<sub>3</sub>C [Joint Committee on Powder Diffraction Standards (JCPDS) no. 35-0772].<sup>35</sup> The two notable peaks appeared at 53.5 and 75.8°, which could be attributed to Fe<sub>3</sub>N (112) and (113) phases, respectively (JCPDS no. 01-072-2125).<sup>36,37</sup> Also, it is worth noting that there was no peak corresponding to metallic iron in the XRD profile of the FeHCNR, and thus, it could be confirmed that the post-synthesis acid washing ensured the removal of the unreacted metal impurities from the system. Metal-related peaks in the XRD pattern implies the absence of Fe atomic dispersion.<sup>38</sup> The XRD characterization discloses that the iron in the FeHCNR contains mixed phases of Fe<sub>3</sub>C and Fe<sub>3</sub>N. The existence of both these iron moieties together can help the system acquire the bifunctional characteristics to work as an efficient electrocatalyst for facilitating the HER and ORR. The XRD pattern of the ZnONR is in good agreement with the standard ZnO patterns (JCPDS no. 36-1451). On comparing the XRD profile of the FeHCNR with that of the ZnO template, it could be observed that there are no common peaks

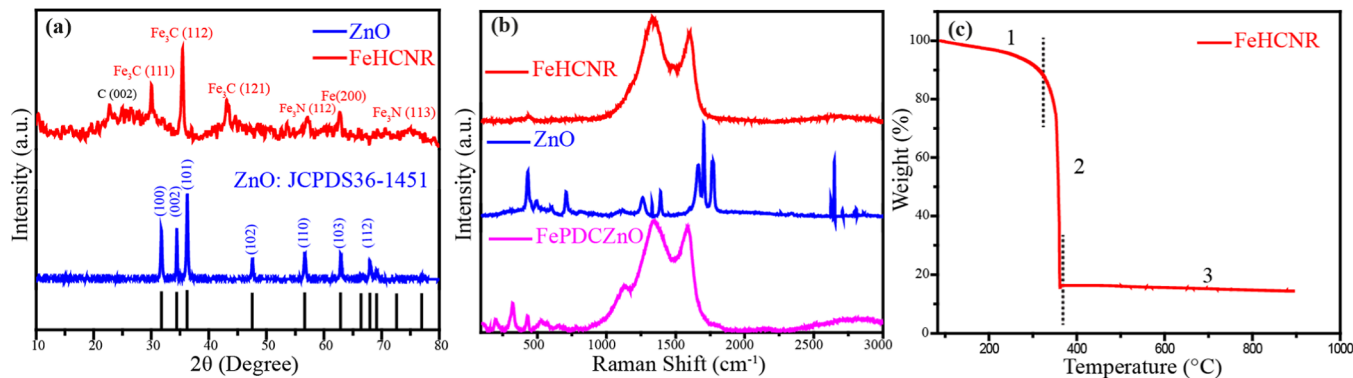


**Figure 2.** (a) XRD patterns of ZnO and the FeHCNR; (b) comparison of the Raman spectra of the FeHCNR, ZnO, and FePDCZnO; and (c) TGA profile of the FeHCNR.

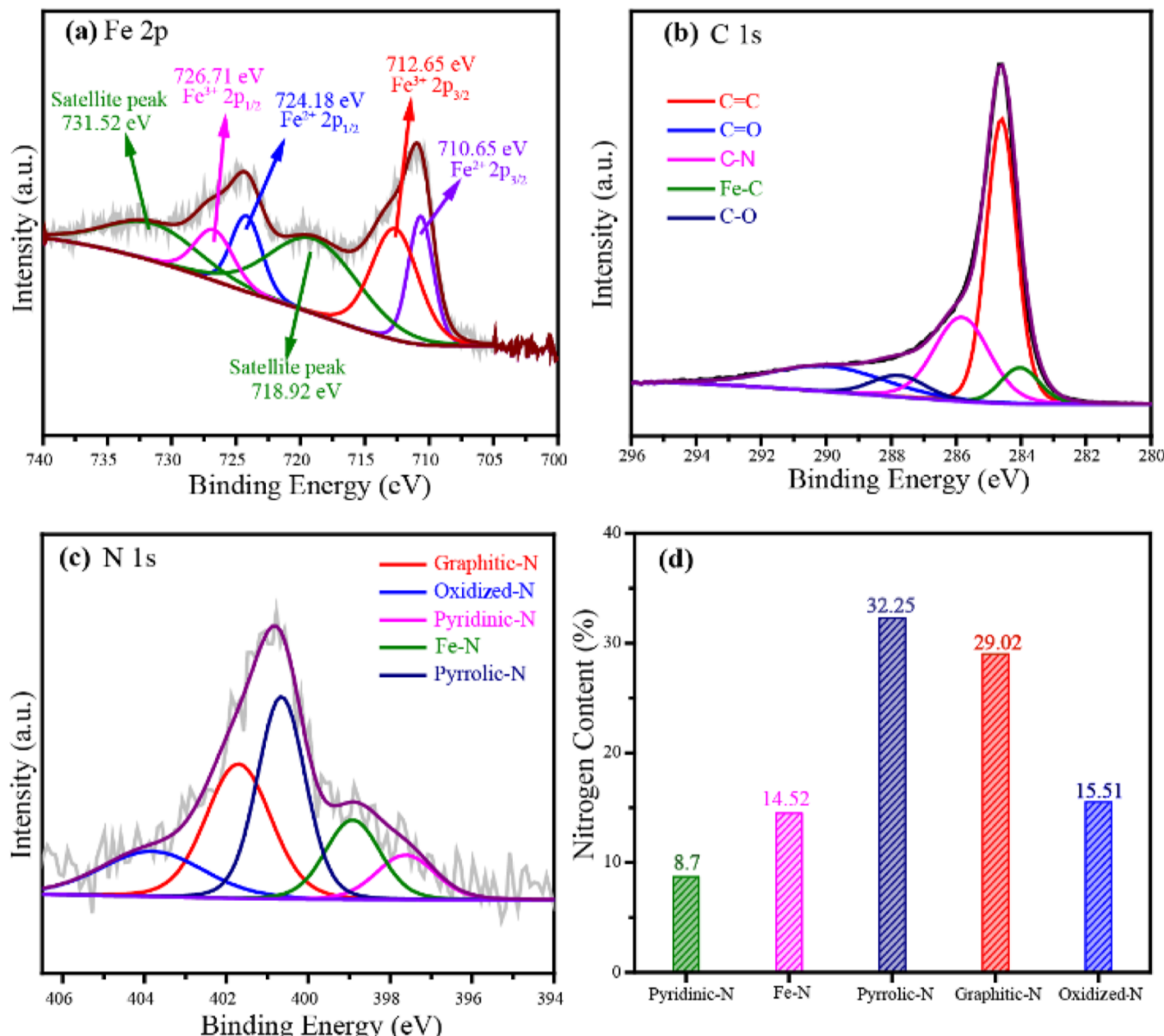


**Figure 3.** Deconvoluted (a) Fe 2p, (b) C 1s, and (c) N 1s XPS spectra of the FeHCNR and (d) bar diagram representing the different types of nitrogen and their atomic percentages obtained from the N 1s spectrum of the FeHCNR.

in both the samples, and this proves the successful removal of the ZnO template by the NH<sub>4</sub>Cl-assisted leaching method.

The degree of graphitization of the material considerably impacts the electrical conductivity of the system, which is

essential in delivering electrocatalytic performance. The Raman spectral analysis is being widely performed to understand the structural information regarding distorted, graphitic, amorphous, or crystalline carbon phases present in the system. The bond stretching of the  $sp^2$ -hybridized carbon atoms of the hexagonal graphitic rings causes the G band to emerge at  $1594\text{ cm}^{-1}$ , while the D band at  $1344\text{ cm}^{-1}$  results from the distorted carbon frames on the defect sites. In the proportionality term, the ratio of the intensities of the D band to the G band ( $I_D/I_G$ ) provides information about the degree of distortion of the carbon structure; with the increase in the degree of distortion, the  $I_D/I_G$  increases. The catalyst shows an  $I_D/I_G$  ratio of 1.20, implying a greater disorder (Figure 2b). High heteroatom loading, such as nitrogen, is known to cause stress in the lattice, resulting in increased disorder in the system.<sup>39,40</sup> Also, the observed broad D band, as compared to that of the reported carbon nanotubes, may be ascribed to the development of an amorphous porphyritic carbon layer on the surface.<sup>41</sup> The Raman spectra of the ZnO nanotube and FePDCZnO are also shown in Figure 2b. A strong and narrow peak is seen at  $437\text{ cm}^{-1}$ , which has been allocated to one of the two E2 modes relating to the important feature of the Zn motion of the Wurtzite phase of ZnO.<sup>42</sup> Along with this, a weak band corresponding to the E1 mode of ZnO accompanied by the deficiency of oxygen is appeared at  $530\text{ cm}^{-1}$ .<sup>43</sup> The other associated characteristic peaks of ZnO appeared at  $583$  and  $738\text{ cm}^{-1}$  are ascribed to the E1 and B1 modes, respectively.<sup>44</sup> However, it should be noted that the peaks corresponding to Zn are completely absent in the case of the FeHCNR, implying the complete removal of Zn through the  $\text{NH}_4\text{Cl}$  treatment.

The amount of the inorganic residue originating from the FeHCNR was measured by TGA in the oxygen environment. The TGA profile recorded in the  $\text{O}_2$  atmosphere for the catalyst (Figure 2c) represents three distinct weight loss regions. The weight reduction between 100 and  $280\text{ }^\circ\text{C}$  in the thermogram is ascribed to the decomposition and dehydration of the functional groups present on the carbon surface.<sup>45</sup> The second weight loss region corresponds to the combustion of amorphous and microcrystalline carbon.<sup>46</sup> The final residue is calculated to be about 14.6 wt %, which is attributed to the total amount of iron in the system. The TGA curve of the material before the leaching of the ZnO template has also been carried out in an inert atmosphere. As seen in the thermogram presented in Figure S4, there is a small weight reduction below  $250\text{ }^\circ\text{C}$  corresponding to the evaporation of water molecules. As the temperature is increased, the weight is gradually reduced up to 91%, which suggests that FePDCZnO is stable at higher temperatures. ICP-OES analysis was also conducted (Table S1) to obtain the exact metal loading in the FeHCNR catalyst, and an Fe content of 14.9% has been estimated in the system.

The elemental compositions and chemical states of the FeHCNR were analyzed using X-ray photoelectron spectroscopy (XPS) studies, which would have a direct impact on the electrochemical performance of the catalyst.<sup>47–49</sup> The XPS survey spectra of the FeHCNR are shown in Figure S5, confirming the existence of C, N, O, and Fe elements. The assessed atomic percentages of C, N, O, and Fe are 88.49, 2.85, 7.08, and 1.58%, respectively. These outcomes uphold the results of the elemental composition derived from the SEM-energy-dispersive X-ray spectroscopy analysis (Figure S6). The deconvoluted Fe 2p XPS spectrum for the FeHCNR (Figure 3a) shows noticeable peaks positioned at 726.7 and  $724.2\text{ eV}$ ,

which are assigned to Fe  $2p_{1/2}$  of Fe(III) and Fe(II), respectively.<sup>50</sup> The other two peaks appearing at the binding energies of 712.6 and  $710.6\text{ eV}$  are attributed, respectively, to the  $2p_{3/2}$  state of Fe(III) and Fe(II).<sup>51</sup> Also, their corresponding satellite peaks appeared at 731.5 and  $718.9\text{ eV}$ .<sup>52</sup> This result indicates the coexistence of Fe(II) and Fe(III) atomic states in the FeHCNR.<sup>53,54</sup> The existence of the Fe– $N_x$  bonding, which accounts for a considerable fraction of the overall Fe content, is shown by the weak doublets for the Fe  $2p_{3/2}$  signals appearing at 710.6 and  $712.6\text{ eV}$ .<sup>18,55,56</sup> The deconvoluted C 1s XPS spectrum of the catalyst (Figure 3b) shows five peaks. The  $sp^2$ -hybridized graphite-like carbon atoms (C=C) are responsible for the main peak at  $284.6\text{ eV}$ .<sup>57</sup> The C–O and C=O species are represented by the other peaks at  $287.7$  and  $289.2\text{ eV}$ , respectively.<sup>58</sup> The peak centered at  $286.3\text{ eV}$ , which is attributed to the C–N bond, serves as valid evidence of the incorporation of N heteroatoms in the carbon lattice. This has a significant impact on the electrochemical performance of the systems.<sup>59</sup> Along with this, the relatively high content of the  $sp^2$ -hybridized carbon (55.7 at. %) verifies the high degree of graphitization, which also is an important performance deciding parameter. The degree of graphitization directly relates to the electrical conductivity, and better graphitization helps reduce the  $iR$  drop during the current ( $i$ )–voltage ( $V$ ) polarization experiments. Apart from the previously mentioned carbon XPS peaks, a peak with low intensity is observed at  $284.9\text{ eV}$ . This peak is attributed to the iron–carbon coordination and points toward the formation of a small extent of iron carbides during the high-temperature annealing process.

Furthermore, the high-resolution N 1s spectrum (Figure 3c) was deconvoluted into five peaks corresponding to the pyridinic N (397.6 eV), Fe–N (398.9 eV), pyrrolic N (400.6 eV), graphitic N (401.7 eV), and oxidized N (403.8 eV) states present in the catalyst matrix.<sup>60,61</sup> The quantitative depiction of all the distinct forms of nitrogen species present in the catalyst is shown in Figure 3d as a bar diagram. The nitrogen atoms doped at the margins of the graphitic carbon layers are represented by the pyridinic nitrogen.<sup>62,63</sup> Besides, the lone pairs of electrons of the pyrrolic nitrogen and pyridinic atoms help form the Fe– $N_x$  active sites.<sup>64–66</sup> As the binding energies of Fe–N and pyridinic nitrogen are so close, the peak at 398.9 eV also includes an input from the nitrogen bound with the Fe atoms.<sup>67–69</sup> The graphitic N is characterized as that which is doped inside the graphitic carbon plane, whereas the pyrrolic N is defined as that which is doped within a five-membered heterocyclic ring.<sup>70,71</sup> The quantification mapping confirms that the nitrogen atoms are effectively doped in the carbon framework by substituting the carbon atoms situated both at the edges and within the graphitic carbon layers. Earlier reports show that nitrogen's high electron affinity property in the carbon layer can bring a positive charge density on the neighboring C atoms, enabling oxygen adsorption and, thereby, weakening the bonding of the oxygen molecule.<sup>72,73</sup> Both the graphitic N and pyridinic N have been found to play crucial roles in enhancing the ORR activity. The greater current density, spin density, and density of the  $\pi$  states of the C atoms around the Fermi level can all be attributed to the high pyridinic N content.<sup>74,75</sup> Also, graphitic N is unequivocally identified with the ability to facilitate the ORR through the favorable four-electron (4e<sup>-</sup>) transfer process.<sup>59,76</sup>

The BET surface area and total pore volume of the FeHCNR and FePDCZnO counterpart were measured from

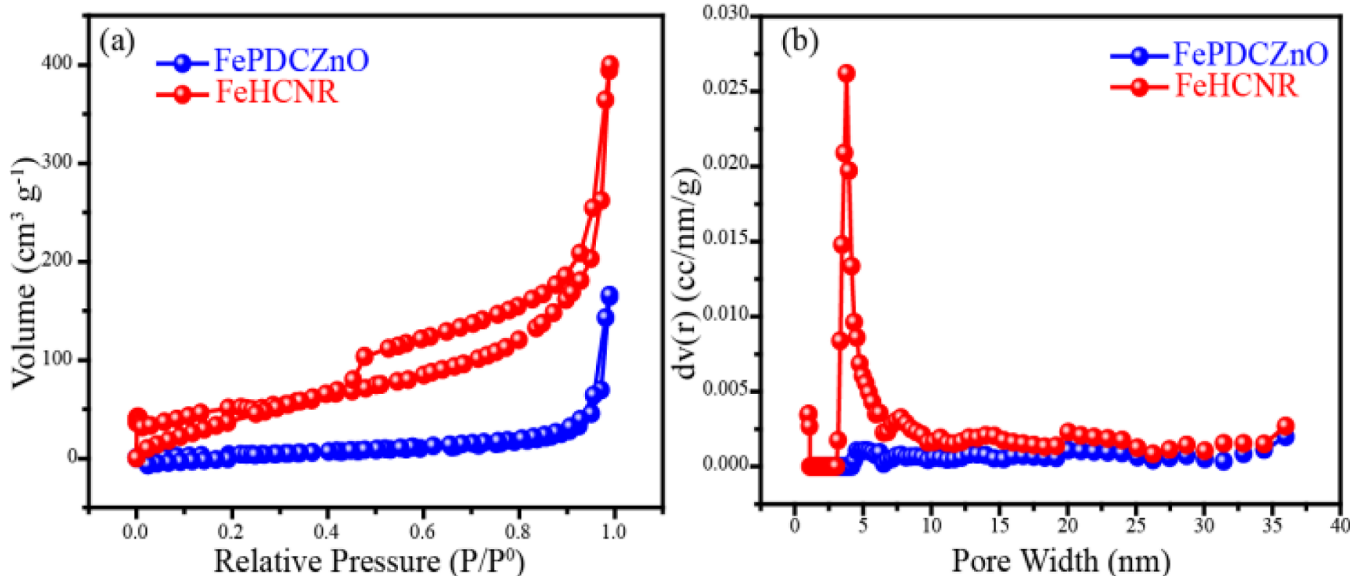


**Figure 4.** (a) BET isotherms and (b) pore size distribution profiles of FePDCZnO and the FeHCNR.

the nitrogen adsorption–desorption analysis. Figure 4a shows the  $\text{N}_2$  adsorption–desorption isotherms of the FeHCNR and FePDCZnO, which show typical type-IV characteristics, indicating the materials’ dominant mesoporosity. Figure 4b shows the pore size distribution patterns of the FeHCNR and FePDCZnO. The FeHCNR has a high density of pores in the region of 3.0–4.5 nm, indicating that the system is mesoporous. The FeHCNR has a BET surface area of  $203 \text{ m}^2 \text{ g}^{-1}$  and a total pore volume of  $0.43 \text{ cm}^3 \text{ g}^{-1}$ , while FePDCZnO has a surface area of  $21.3 \text{ m}^2 \text{ g}^{-1}$  and a total pore volume of  $0.12 \text{ cm}^3 \text{ g}^{-1}$  (Table S2). In comparison to its non-hollow counterpart, FePDCZnO, the FeHCNR exhibits the desired mesoporous structure with a 9 times higher surface area and a large pore volume. These results suggest that introducing and then removing the ZnO nanorod template can significantly increase the specific surface area of the catalyst. The high surface area benefits in terms of a wider exposure of the catalytically active sites, and the mesoporous texture can provide facile channels for transporting gas molecules and diffusion of ions during the HER and ORR processes.<sup>67</sup>

**Hydrogen Evolution Reaction.** In a 0.5 M  $\text{H}_2\text{SO}_4$  solution, the electrochemical activities of the as-prepared materials were initially investigated for the HER using an RDE setup connected to a potentiostat (BioLogic SP-300). The working electrode was a glassy carbon electrode with a working area of  $0.196 \text{ cm}^2$  coated with the FeHCNR. A graphite rod and  $\text{Hg}/\text{HgSO}_4$  were used as the counter electrode and reference electrode, respectively, throughout the electrochemical analysis. At a scan rate of  $10 \text{ mV s}^{-1}$ , linear sweep voltammetry (LSV) was performed in a  $\text{N}_2$ -saturated 0.5 M  $\text{H}_2\text{SO}_4$  solution. Before the LSV measurements, to stabilize and activate the electrocatalyst, about 50 cycles of cyclic voltammetry (CV) were performed with a scan rate of  $30 \text{ mV s}^{-1}$  in the potential window of  $-0.15$  to  $0.15 \text{ V}$  (vs the reversible hydrogen electrode, RHE). All the LSV measurements were executed with 90% iR correction. Figure 5a shows the HER data for all of the as-synthesized catalysts as well as the state-of-the-art Pt/C (20%) catalyst. As displayed in Figure 5a, the ZnO template used for the preparation of the FeHCNR shows negligible activity toward the HER. To achieve a current

density of  $50 \text{ mA cm}^{-2}$ , the catalyst synthesized without the use of a template (FePDC) has shown an overpotential value of  $172 \text{ mV}$  and the hollow carbon nanorod material without iron doping (HCNR) has displayed an overpotential of  $117 \text{ mV}$ . The higher overpotential value of FePDC indicates that the hollow structure of the HCNR helps the facile access of the active sites by the reactants, thereby increasing the rate of evolution of hydrogen. FePDCZnO (the material having the ZnO template) exhibits an overpotential value of  $75.5 \text{ mV}$  at  $50 \text{ mA cm}^{-2}$ . It is worth noting that the material derived after the ZnO template removal (i.e., FeHCNR) has excellent performance characteristics, with an overpotential of only  $29.4 \text{ mV}$  at a current density of  $50 \text{ mA cm}^{-2}$ . It is to be noted that the performance of the FeHCNR is nearly comparable to that of the state-of-the-art Pt/C catalyst, which requires an overpotential of  $18.2 \text{ mV}$  to achieve the benchmark current density of  $50 \text{ mA cm}^{-2}$ . As a result, the FeHCNR has been identified as one of the best transition metal-based electrocatalysts for the HER in acidic media (Table S3). The HER activity of the catalysts, as well as the overpotential values taken from the LSV data, are given in the form of a bar diagram in Figure 5b to allow for easy quantitative comparison. The high performance of the FeHCNR in comparison to that of its non-hollow counterpart FePDCZnO underlines the critical role played by the favorable hollow morphological features of the former in simultaneously addressing the key requirements such as the active site accessibility by the reactants and their effective utilization during the electrode process. Furthermore, the mass activity and specific activity of the electrocatalysts toward the HER were calculated at the overpotential value of  $50 \text{ mV}$  (Figure S9a). As expected, the FeHCNR recorded the highest mass activity and specific activity for the HER compared to the other samples. Electrochemical impedance spectroscopy (EIS) is utilized to explore the improved activity of the FeHCNR for the HER. EIS is a vital tool for determining the ionic resistance and the charge transfer characteristics of the catalyst material during the HER. For this reason, EIS was performed with a frequency range of 200 kHz to 100 MHz and an AC amplitude of  $10 \text{ mV}$  in a 0.5 M  $\text{H}_2\text{SO}_4$  solution at a potential of  $0.30 \text{ V}$  (vs RHE). From the obtained

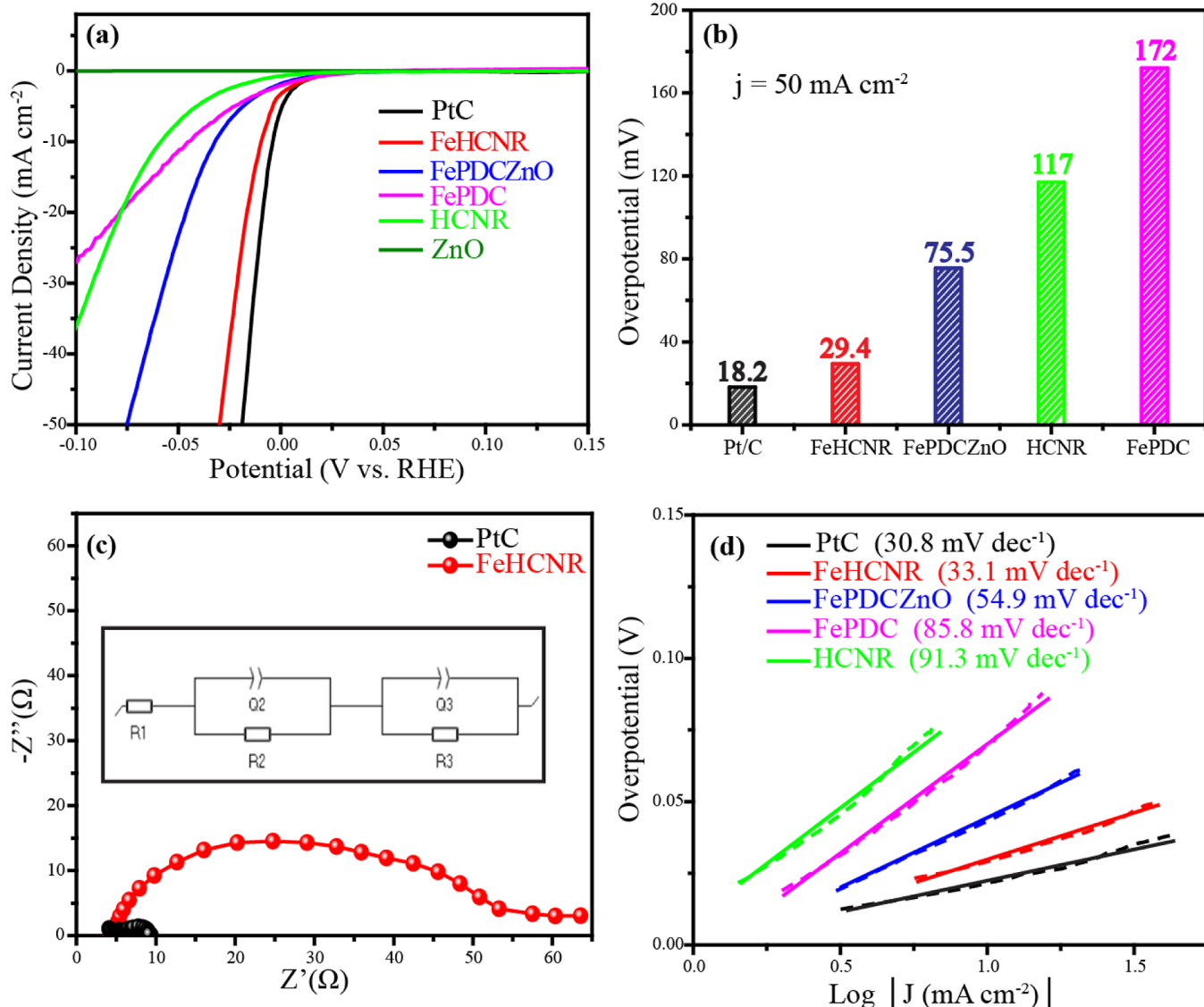


**Figure 5.** (a) Comparative LSV curves recorded for the HER, (b) bar diagram indicating the overpotential recorded at a current density of  $50 \text{ mA cm}^{-2}$  corresponding to the HER on the different tested samples, (c) Nyquist plots recorded on the samples, with the inset showing the equivalent circuit used to fit the data, and (d) comparison of the Tafel plots representing the intrinsic activities of the catalysts toward the HER.

Nyquist plots in Figure 5c and those of other comparative samples in Figure S7, the charge transfer resistance ( $R_{\text{CT}}$ ) values of FeHCNR and PtC (20%) catalysts have been determined. The equivalent circuit provided in the inset of Figure 5c is used to fit the Nyquist plot, where R<sub>1</sub>, R<sub>2</sub>, and R<sub>3</sub> represent the resistance and Q<sub>1</sub> and Q<sub>2</sub> represent the constant phase components. The  $R_{\text{CT}}$  values are obtained from the difference between R<sub>2</sub> and R<sub>3</sub>. The  $R_{\text{CT}}$  values of ZnO, FePDA, and FePDCZnO are significantly high in the range of 1000 to 4000  $\Omega$ . However, both the FeHCNR and Pt/C show considerably lower  $R_{\text{CT}}$  values of 55 and 10  $\Omega$ , respectively. The lower  $R_{\text{CT}}$  value of the FeHCNR indicates that the electrons are transported rapidly during the gas evolution reaction, which makes it more active toward the HER than the other catalysts. The lower  $R_{\text{CT}}$  value eventually improves the HER kinetics, thereby enhancing the catalytic activity. The electrocatalytic kinetics and mechanism of the HER are explored with the aid of Tafel plots. Figure 5d displays the Tafel plots of all the prepared materials along with those of the commercial Pt/C (20%) catalyst. The catalyst with a lower

Tafel slope designates the higher reaction kinetics with increasing applied potential. FePDC, HCNR, and FePDCZnO exhibit Tafel slope values of 85.8, 91.3, and 54.9  $\text{mV dec}^{-1}$ , respectively. However, the FeHCNR shows a Tafel slope value of 33.1  $\text{mV dec}^{-1}$ , which is very much close to that of the benchmark Pt/C catalyst (30.8  $\text{mV dec}^{-1}$ ), demonstrating a similar HER kinetics on both systems. The value of the Tafel slope in the case of the FeHCNR forecasts the involvement of the Volmer reaction pathway in the rate-determining step.<sup>77</sup> The key factor that plays a crucial role in the better HER activity of the FeHCNR is its hollow nanorod morphology, which provides better exposure of the active sites to facilitate the reaction. Also, the open-tube cavity structure of the catalyst supports the electrolyte diffusion and, successively, the hydrogen gas produced. Also, the high-temperature annealing provides better electrical conductivity, which enables faster kinetics during the reaction by minimizing the  $iR$  drop under the experimental conditions. In addition to the higher activity, the operational stability of the electrocatalyst in the corrosive environment is an important criterion for assessing the

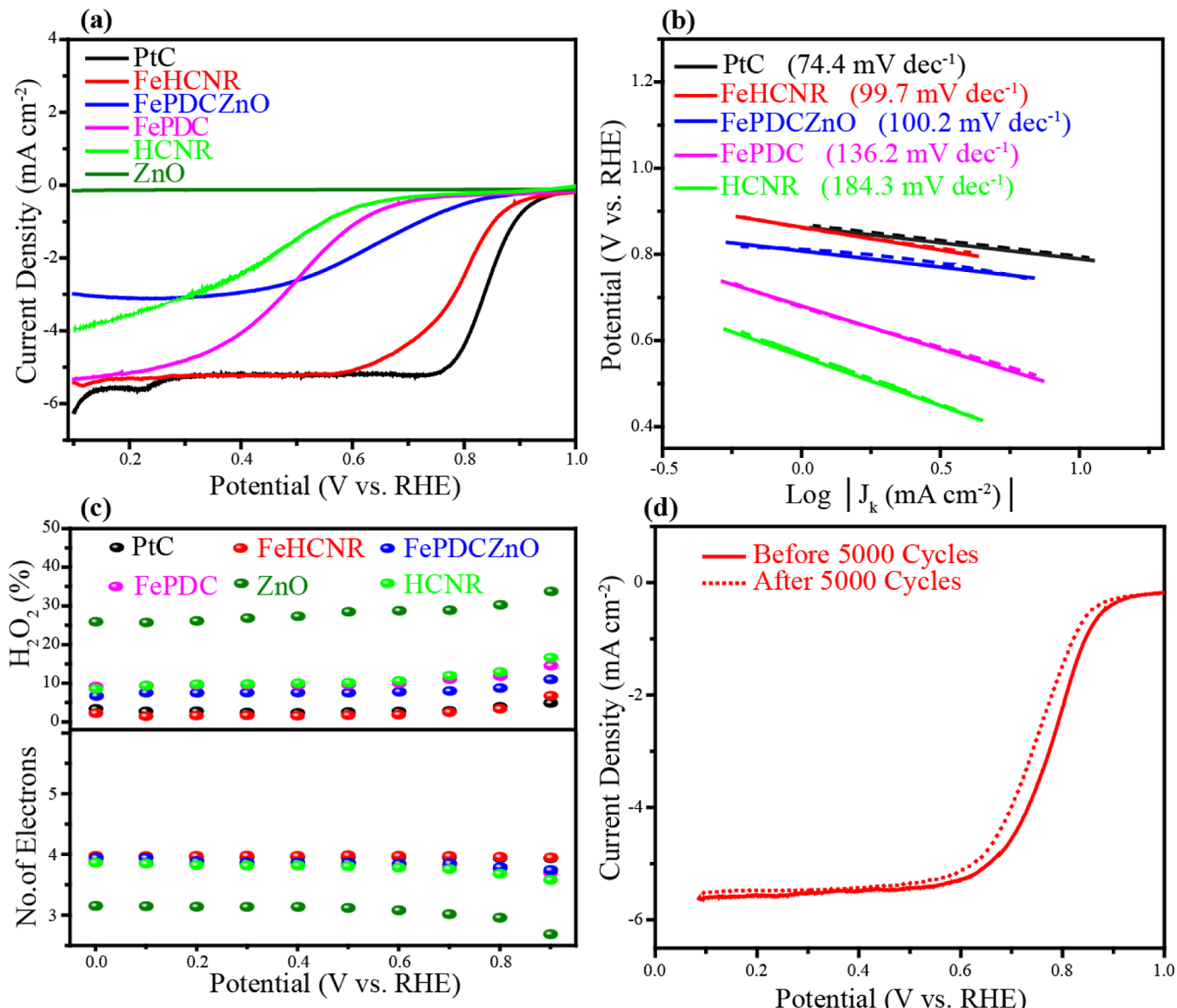


**Figure 6.** (a) Comparative LSV curves corresponding to the ORR in an acidic environment of all the catalysts, (b) Tafel plot comparison of all the catalysts, (c) amount of H<sub>2</sub>O<sub>2</sub> generated during the ORR calculated as a function of the electrode potential (above) and the electron transfer number (*n*) for the ORR, as calculated from the RRDE analysis (below), and (d) LSV comparison of the FeHCNR performed before and after the 5000 ADT cycles.

efficiency of the catalyst. This was evaluated by the chronoamperometric analysis of the FeHCNR in a N<sub>2</sub>-purged 0.5 M H<sub>2</sub>SO<sub>4</sub> solution at a current density of 50 mA cm<sup>-2</sup> for 12 h, and the resulting data are shown in Figure S8. It is evident from the figure that the system performs consistently over a 12 h investigation period under high current density conditions, with no degradation in the current output. The chronoamperometry analysis thus validates the higher structural integrity of the FeHCNR for the HER.

**Oxygen Reduction Reaction.** In addition to serving as a remarkable HER electrocatalyst in acidic media, the FeHCNR was found to exhibit good ORR performance in an acidic environment. To evaluate the ORR performance of the catalyst, LSV polarization analysis was performed on an RDE at 1600 rpm of the working electrode and 10 mV s<sup>-1</sup> in an O<sub>2</sub> saturated 0.5 M H<sub>2</sub>SO<sub>4</sub> electrolyte. The LSV curves of all the samples and the state-of-the-art 40 wt % Pt/C catalyst are shown in Figure 6a. The onset potential and half-wave

potential ( $E_{1/2}$ ) of the bulk FePDC catalyst, which is prepared without any template, are 0.75 and 0.49 V against RHE, respectively, indicating minimal ORR activity. The hollow carbon nanorod material without iron doping (HCNR) has shown an onset potential of 0.70 V and  $E_{1/2}$  of 0.45 V versus RHE. On the other hand, FePDCZnO with the rod-like morphology exhibits better ORR performance than the bulk-phase FePDC catalyst. FePDCZnO exhibits the potential values of 0.93 and 0.64 V versus RHE, respectively, for the onset and half-wave potentials. The relatively higher activity of the nanorod morphology than that of its bulk counterpart is attributed to the better exposed active sites due to the confined growth of the FePDC phase on the ZnO nanorod surface. Further, upon removing the ZnO template, additional active sites present on the inner side are also getting exposed, thereby enabling the FeHCNR to record the highest onset potential of 0.97 V and  $E_{1/2}$  of 0.79 V versus RHE among the three systems. It should be noted that the values recorded on the

FeHCNR closely match with those on the state-of-the-art Pt/C catalyst, which has an onset potential and an  $E_{1/2}$  of 0.99 and 0.84 V versus RHE, respectively. The mass activity and specific activity toward the ORR were calculated at a potential 0.70 V versus RHE, and the data are depicted as a bar diagram in Figure S9b. Both the mass activity and specific activity of the catalysts follow the order corresponding to the LSV profiles of the ORR. The FeHCNR is also competitive with the other recently reported similar electrocatalysts with respect to the performance toward the ORR (Table S4).

The Nyquist plots recorded on the synthesized samples in the O<sub>2</sub>-saturated 0.5 M H<sub>2</sub>SO<sub>4</sub> electrolyte at the corresponding onset potentials, with a rotation rate of 1600 rpm of the working electrode, are depicted in Figure S10. The FeHCNR exhibited the smallest radius of the semicircle and, thus, the smallest charge transfer resistance ( $R_{CT}$ ) among all the prepared materials. The smaller value of  $R_{CT}$  favors the fast movement of ions, thereby encouraging the enhanced ORR kinetics. The  $R_{CT}$  value of the FeHCNR, FePDCZnO, FePDC, and ZnO are 21, 863, 970, and 2200 Ω, respectively. The FeHCNR has a lower  $R_{CT}$  value, which indicates that it has better conductivity, allowing for faster electron transport across the system. The increase in the conductivity of the system is due to defects generated by the iron-coordinated active centers, N doping, and high-temperature pyrolysis. The Tafel slopes were used to determine the kinetic parameters of the as-prepared materials. As presented in Figure 6b, the FeHCNR exhibited a smaller Tafel slope (99.7 mV dec<sup>-1</sup>) than FePDCZnO (100.2 mV dec<sup>-1</sup>) and FePDC (136.2 mV dec<sup>-1</sup>). The Tafel slope value of Pt/C is found to be 74.4 mV dec<sup>-1</sup>. The structure-favored advantages of the FeHCNR with respect to faster electron transfer and active site exposure are thought to favor the ORR.<sup>78</sup>

The double-layer capacitance ( $C_{dl}$ ) in the non-Faradaic region gives insights into the electrochemical active surface area (ECSA) for the platinum-free systems in the catalyst interface.<sup>79</sup> The ECSA is directly proportional to the  $C_{dl}$  value, as expressed below

$$\text{ECSA} = \frac{C_{dl}}{C_s}$$

where  $C_s$  represents the specific capacitance of the element. To quantify the density of electrochemical active sites, the  $C_{dl}$  values of all the catalysts were compared. The  $C_{dl}$  was calculated using cyclic voltammograms recorded at various scan rates of 5, 10, 20, 40, 60, 80, 100, and 120 mV s<sup>-1</sup> in the non-Faradaic region (1.05 to 1.15 V vs RHE) (Figure S11a-d). The scan rate is plotted against the anodic peak current density at 1.10 V (vs RHE), and the result is a straight line (Figure S11e). The  $C_{dl}$  value is directly related to the slope of the as-obtained straight line.<sup>80</sup> The FeHCNR catalyst has shown a  $C_{dl}$  value of 4.6 mF cm<sup>-2</sup>, which is very much higher than that of the other comparative samples, with values of 1.6, 0.55, and 0.18 mF cm<sup>-2</sup> for FePDCZnO, FePDC, and ZnO, respectively. The higher  $C_{dl}$  value of the FeHCNR is due to the hollow cavity and mesoporous structure of the system, allowing a large number of active sites to be exposed. The prepared materials and the Pt/C catalyst have been subsequently evaluated to understand their selectivity toward oxygen reduction involving the preferred four-electron (4e<sup>-</sup>) reduction mechanism. This has been evaluated by employing an RRDE to measure the hydrogen peroxide (H<sub>2</sub>O<sub>2</sub>) yield, which is the product formed

from the undesirable two-electron (2e<sup>-</sup>) reduction process. The RRDE measurement was carried out in an O<sub>2</sub>-saturated 0.5 M H<sub>2</sub>SO<sub>4</sub> electrolyte at a scan rate of 10 mV s<sup>-1</sup> with the electrode rotation speed of 1600 rpm. By analyzing the ring and disc currents, the number of electrons ( $n$ ) transferred during the reaction and the percentage of H<sub>2</sub>O<sub>2</sub> generated were estimated (Eqs S1 and S2, Supporting Information). Figure 6c shows the comparative RRDE results of the prepared materials and the state-of-the-art Pt/C catalyst. In a wide potential range of 0–0.90 V (vs RHE), the FeHCNR produced a low H<sub>2</sub>O<sub>2</sub> yield of 2.5% and a high “ $n$ ” value of 3.97. In other words, the FeHCNR has high selectivity, allowing it to promote a direct 4e reduction process that results in H<sub>2</sub>O as the major product in this potential range. It should be noted that this value of H<sub>2</sub>O<sub>2</sub> yield obtained from the FeHCNR is nearly comparable to that measured on Pt/C, which displays a value of 3.0%. On the other hand, the control samples FePDCZnO, FePDA, and ZnO have displayed H<sub>2</sub>O<sub>2</sub> yields of 8, 10.4, and 28.2%, respectively. Thus, kinetically, the FeHCNR could display a close matching performance with Pt/C for the ORR, which points toward the favorable intrinsic activity characteristics incurred by the Fe–N based active sites residing on the in-house system. This has been substantiated with the morphological advantages of the system due to its benefits in terms of enhanced mass transport of the reactants and better accessibility to the active sites.

In addition to the improved ORR activity, it is significant to evaluate the catalyst's stability in an electrochemical environment to ensure its potential for real-world applications in realistic device-level explorations. The stability tests were carried out by extensively cycling the potential between 0.60 and 1.0 V versus RHE at 100 mV s<sup>-1</sup> in O<sub>2</sub>-saturated electrolytes and subsequently quantifying the change in the  $E_{1/2}$  values after the corrosive accelerated durability test (ADT). The set triggered conditions for the ADT can degrade the carbon surface and dopants along with the catalytically active metal centers. As shown in Figure 6d, the FeHCNR exhibits excellent stability even after the ADT, as can be reflected from the negative shift of only 31 mV in  $E_{1/2}$  after the 5000 cycles. This is a much superior performance compared to the 100 mV loss reported for the standard polyaniline-derived FeN<sub>x</sub> catalysts.<sup>81,82</sup> Also, under the same electrochemical situation, the ADT for the state-of-the-art Pt/C catalyst incurred a 52 mV decrease in  $E_{1/2}$  (Figure S12). The huge difference discovered in the instance of Pt/C could be due to the Pt nanoparticles detaching and agglomerating from the carbon support. Contrary to this, in the case of the FeHCNR, Fe–N<sub>x</sub> active sites are well-connected to the carbon framework and are considered to be very stable against leaching or aggregation during the potential cycling. For the assessment of the structural stability of the catalyst, XRD analysis was carried out after the ADT. We have coated the FeHCNR over a GDL and performed the 5000 cycles of the ADT in the ORR region (0.60 to 1.0 V vs RHE). Further, the GDL was subjected to XRD analysis. For the comparison purpose, the XRD analysis of the bare GDL and FeHCNR-coated GDL was conducted prior to the ADT. Figure S13a illustrates the comparative XRD patterns of all the three samples. As the materials are coated over the GDL, a high-intensity peak at 26° (002) and a peak at 54° (004) appear in all the three samples corresponding to the graphitic plane. Along with the graphitic peak, another peak at 18° was observed commonly in all the three samples corresponding to the PTFE present in the GDL.<sup>83</sup> The XRD

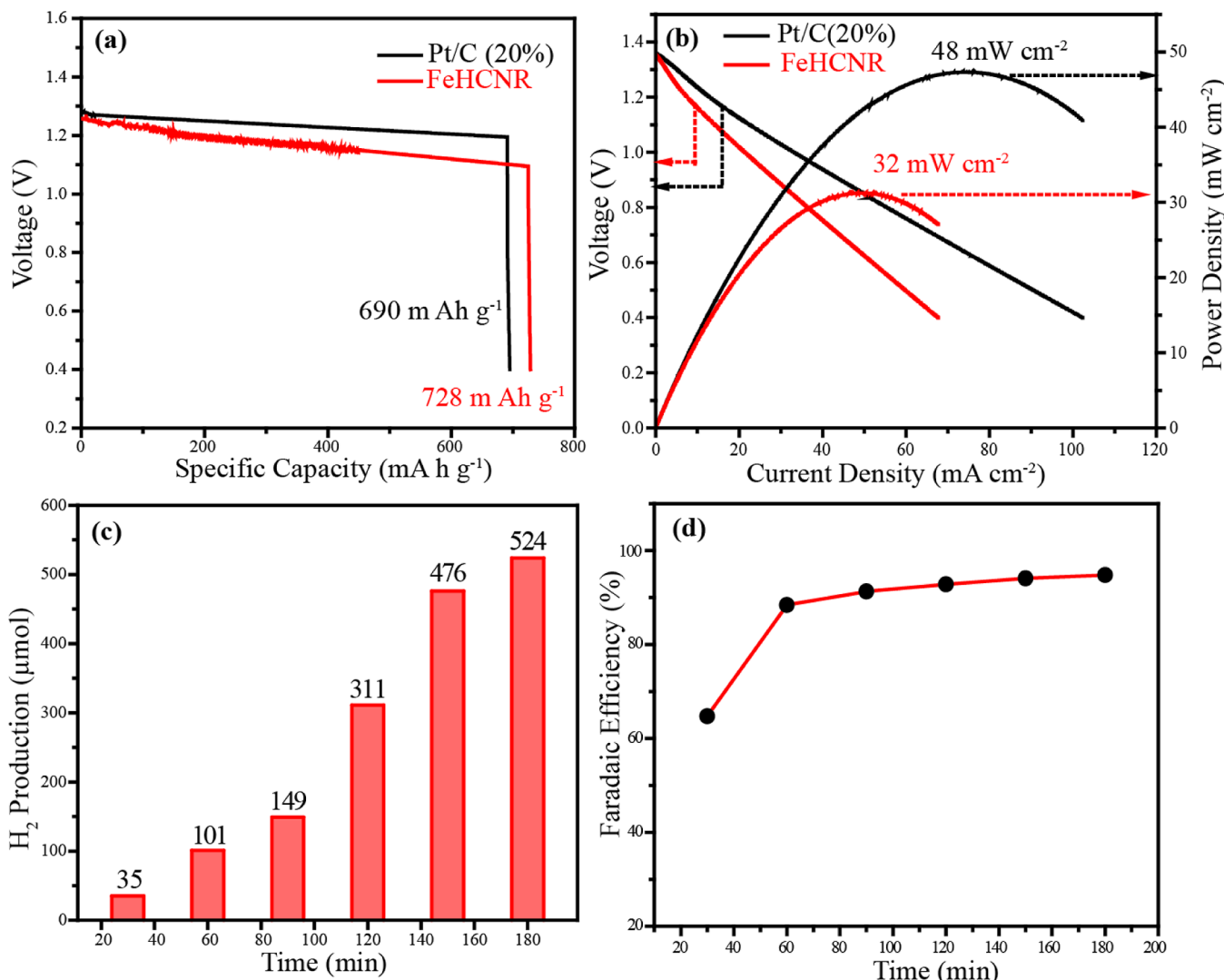


**Figure 7.** (a) Plots representing the voltage vs specific capacity of the FeHCNR and Pt/C (20%)-based Zn–H<sub>2</sub> hybrid batteries, (b) voltage (left y-axis)—current density and power density (right y-axis)—current density plots obtained from the FeHCNR- and Pt/C (20%)-based Zn–H<sub>2</sub> hybrid battery systems, (c) hydrogen production as a function of the time recorded at the discharge current density of 5 mA cm<sup>-2</sup> and (d) corresponding Faradaic efficiencies calculated for the as-proposed Zn–H<sub>2</sub> hybrid battery as a function of the time.

profile of the FeHCNR before the ADT shows the peaks for (111), (112), and (121) planes of Fe<sub>3</sub>C. The position and intensity of all the peaks were found to be retained after the ADT. The TEM analysis of the FeHCNR was performed after the 5000 cycles of the ADT, and the results are provided in Figure S13b. It is clear from the TEM images that the nanorod morphology is retained even after the 5000 ADT cycles, which highlights the high structural integrity possessed by the catalyst. Further, the XPS analysis of the FeHCNR catalyst is performed to identify the changes incurred in the chemical structure by the ADT. Figure S13c,d represents the O1s XPS spectra of the FeHCNR before and after the ADT, respectively. It could be observed that the percentage of Fe–O is slightly increased from 40 to 45% after the ADT, indicating that Fe<sub>3</sub>C is partially oxidized, leading to the slight degradation of the current after the test. All these post-electrolysis analyses of the catalyst material substantiate its superior stability in the harsh working conditions.

ORR catalysts must have high methanol tolerance since the contaminants in the fuel can poison the active sites. Hence, an anti-methanol poisoning test has been performed for Pt/C and

FeHCNR catalysts by the chronoamperometric response at the half-wave potential of the respective catalyst with a working electrode rotation rate of 1600 rpm in an oxygen-saturated 0.5 M H<sub>2</sub>SO<sub>4</sub> electrolyte with the addition of 3 M methanol. The presence of methanol caused the oxidation on the Pt/C catalyst surface, resulting in a decrease in the oxygen reduction current. This clearly shows that the byproduct generated during methanol decomposition has poisoned the Pt surface.<sup>84</sup> As depicted in Figure S14, methanol addition had no effect on the FeHCNR, showing that the catalyst selectively catalyzes the ORR and is totally resistant to methanol oxidation.

**Alkaline–Acid Zn–H<sub>2</sub> Hybrid Battery.** The FeHCNR brush-coated on the surface of a carbon paper as the cathode with 2 M H<sub>2</sub>SO<sub>4</sub> as the catholyte and a commercial Zn plate as the anode with 4 M NaOH as the anolyte was used to fabricate the alkaline–acid Zn–H<sub>2</sub> hybrid battery (Scheme 1). The energy of Zn oxidation and the electrochemical neutralization of the acid and base can both be collected here (details in the Supporting Information). A BPM separated the anode and cathode chambers to avoid direct neutralization of the anolyte and catholyte with the evolution of heat energy. The

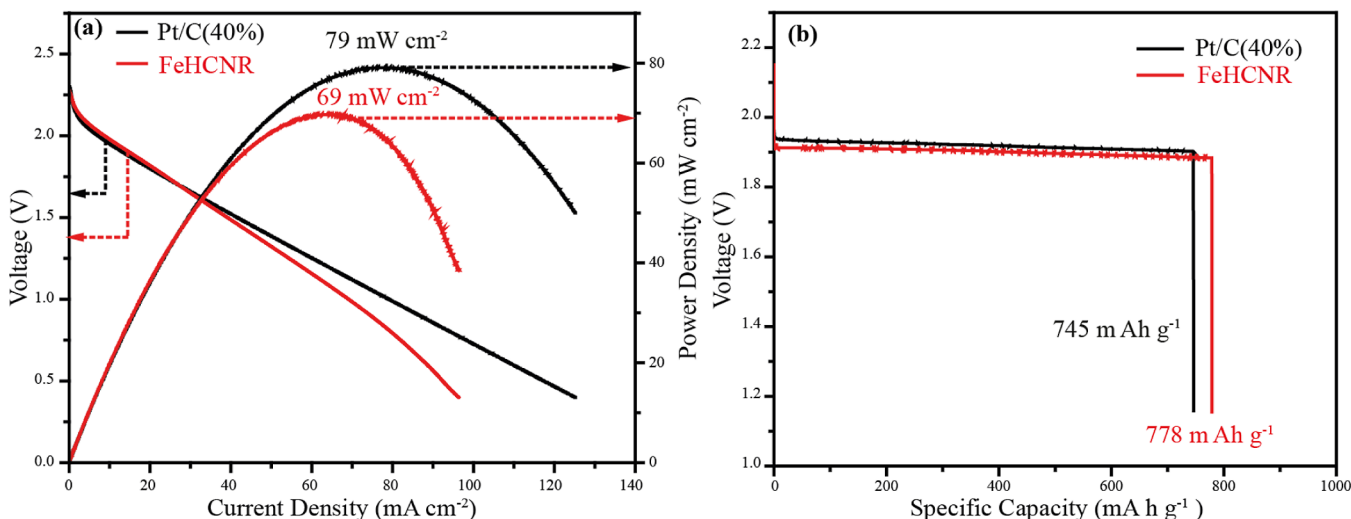
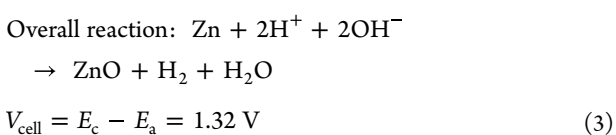
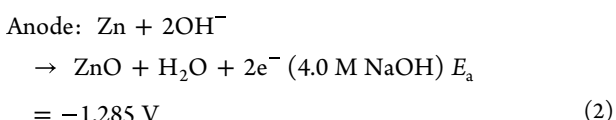
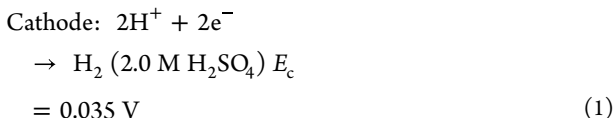


**Figure 8.** (a) Voltage (left y-axis)—current density and power density (right y-axis)—current density polarization plots and (b) voltage vs specific capacity plots of the FeHCNR- and Pt/C (40%)-based AEZAB systems.

commercially available cation exchange and anion exchange membranes were laminated to make the BPM.<sup>85</sup> At the anode, Zn is oxidized in an alkaline solution (eq 1), which is followed by electron transfer through an external circuit, resulting in the release of electrochemical energy. Proton reduces electrochemically by employing this electron, resulting in the HER in the acid medium at the cathode (eq 2). The cation and anion exchange membranes separate  $\text{Na}^+$  and  $\text{SO}_4^{2-}$ , which are then transferred into a water layer; there is no crossover between the two electrode chambers. According to the Nernst equation, the as-developed Zn–H<sub>2</sub> hybrid battery can theoretically provide an open-circuit voltage (OCV) of 1.32 V.<sup>10,12</sup>



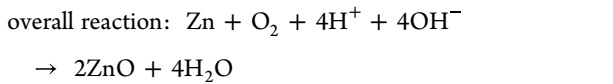
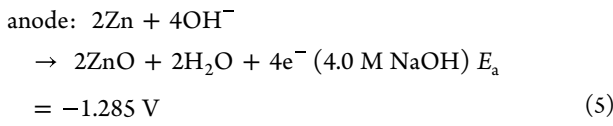
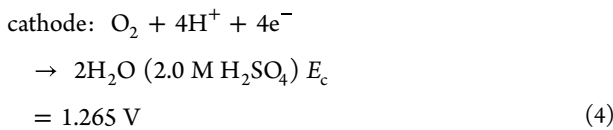
The FeHCNR was engaged as the cathode for the Zn–H<sub>2</sub> hybrid battery based on the half-cell performance results. A system based on a commercial Pt/C-coated cathode was also built for comparison purposes. Both the systems were assembled by removing any dissolved O<sub>2</sub> via N<sub>2</sub> purging. Figure S15 shows the OCVs of 1.26 and 1.29 V, respectively, for the FeHCNR and Pt/C (20%) cathode-based Zn–H<sub>2</sub> hybrid batteries. Because of the overpotential associated with the reactions in the cathode and anode, voltage drops resulting from the two electrolytes, BPM, and contact resistance, and the obtained cell voltage is lower than the theoretical value (1.32 V). The Zn–H<sub>2</sub> hybrid battery was allowed to drag a current density of 5 mA cm<sup>-2</sup>. The comparison of the discharge profiles (Figure 7a) demonstrates the superiority of the FeHCNR over Pt/C in terms of specific capacity. The system

based on the FeHCNR delivered a specific capacity of 728 mA h g<sup>-1</sup>, which is higher than that of its counterpart systems based on Pt/C (690 mA h g<sup>-1</sup>). Furthermore, for the FeHCNR and Pt/C-based systems, the maximum energy densities were estimated to be 903 and 874 W h kg<sup>-1</sup>, respectively. The polarization curve and power density plot for the Zn–H<sub>2</sub> hybrid battery with the FeHCNR cathode catalyst are shown in Figure 7b. The FeHCNR system has a maximum power density of 32 mW cm<sup>-2</sup>, whereas the corresponding system based on Pt/C has a maximum power density of 48 mW cm<sup>-2</sup>.

Gas chromatography was used to record the generated hydrogen volume to illustrate the hydrogen production efficiency during the discharge phase of the hybrid device. A micro syringe (500 μL) was used to collect the generated gas from the headspace and inject it into the gas chromatograph. At a discharge current density of 5 mA cm<sup>-2</sup>, Figure 7c shows the amount of H<sub>2</sub> generated as well as the running time. Thus, this demonstration verifies that the device produces hydrogen and electrochemical energy simultaneously. The calculated and measured hydrogen productions are well-matched, implying a high Faradaic efficiency for H<sub>2</sub> generation. The Faradaic efficiency, which approaches 97% at various operating stages, corroborates this observation (Figure 7d). It should be noted that the low Faradaic efficiency of 65% was obtained at first, which is primarily due to the fact that the H<sub>2</sub> could not leave the carbon paper texture in time and also due to the possibility of the ORR as a side reaction.<sup>10</sup> The FeHCNR-based Zn–H<sub>2</sub> hybrid battery was used to power a 1.2 V light-emitting diode (LED) having a current rating of 20 mA to demonstrate the potential application of the device (Figure S16). Thus, a promising and closely matching performance with that of the Pt/C catalyst could be guaranteed with the demonstration of the hybrid Zn–H<sub>2</sub> hybrid battery by utilizing the in-house catalyst for facilitating the HER in the cathode.

**Asymmetric Electrolyte Zn–Air Battery.** As shown in Scheme 1, an AEZAB was built with NaOH as the anolyte and H<sub>2</sub>SO<sub>4</sub> as the catholyte, both separated by a BPM with the FeHCNR as the cathode catalyst. Theoretically, the AEZAB is capable of producing an output voltage of 2.55 V by utilizing the electrochemical neutralization energy generated from the anolyte and catholyte, which contributes an additional voltage

difference of 0.9 V to the theoretical voltage of the ZAB (1.65 V).<sup>86</sup> The reactions and related calculations of the AEZAB are shown below.<sup>85</sup>



$$V_{\text{cell}} = E_c - E_a = 2.55 \text{ V} \quad (6)$$

On the basis of the ORR half-cell performance, the AEZAB is fabricated by employing the FeHCNR as the cathode; for the purpose of comparison, another cell based on the commercial Pt/C catalyst (40%) was also constructed. The FeHCNR- and Pt/C-based AEZABs display OCV values of 2.15 and 2.18 V, respectively. The obtained cell voltage is lower than the theoretical value, which is likely due to the contribution of the membrane resistance between the two electrode chambers.<sup>87,88</sup> The maximum power density is a significant characteristic to consider when assessing the performance of a ZAB. Figure 8a represents the power density values of the AEZAB systems based on both the catalysts measured by the discharge polarization method. The battery with the FeHCNR cathode achieves a maximum power density of 69 mW cm<sup>-2</sup>, which is nearly identical (79 mW cm<sup>-2</sup>) to that of the counterpart system using the commercial Pt/C cathode catalyst. The specific capacity of the AEZAB systems is derived through the galvanostatic discharge at 10 mA cm<sup>-2</sup> (Figure 8b). The discharge plateaus in the Pt/C- and FeHCNR-based systems are 1.93 and 1.91 V, respectively. The FeHCNR-based AEZAB recorded a specific capacity of 788 mA h g<sup>-1</sup>, which is higher than that of the Pt/C-based cell (745 mA h g<sup>-1</sup>). Furthermore, the energy densities were estimated to be 1438 and 1495 W h kg<sup>-1</sup> for the Pt/C- and FeHCNR-based AEZABs, respectively. For the comparison purpose, a symmetric conventional ZAB (CZAB) was also developed by using 4.0 M NaOH as electrolyte and the FeHCNR as the air electrode. The CZAB displays a low OCV (1.42 V) value compared to the AEZAB; the latter one shows an OCV of 2.18 V. The OCV profiles of both the AEZAB and CZAB recorded for 30 min are presented in Figure S17, where the straight line graph indicates the stability and feasibility of the device. The discharge polarization of the ZAB recorded displays a maximum power density of 30 mW cm<sup>-2</sup> (Figure S18), which is also found to be inferior to that of the corresponding AEZAB system. Thus, the superior OCV and power density of the AEZAB verify that the pH gradient existing between the catholyte and anolyte can significantly contribute to the improvement of the cell performance.<sup>12</sup> This makes AEZAB more promising toward various applications by ensuring an enhanced voltage and power output.

## CONCLUSIONS

A PDA-derived FeHCNR has been prepared by a process involving selected removal of the structure directing template, followed by high-temperature annealing. The hollow structure promotes rapid mass transfer and greater active site exposure, resulting in increased electrochemical activity in the HER and ORR. In a 0.5 M H<sub>2</sub>SO<sub>4</sub> electrolyte, the FeHCNR showed outstanding HER and ORR activities, with an overpotential of 29.4 mV at a current density of 50 mA cm<sup>-2</sup> for the HER and an onset potential of 0.97 V versus RHE for the ORR. Based on the better electrocatalytic activity displayed by the FeHCNR toward the HER, the catalyst has been utilized as the cathode for demonstrating a type of alkaline–acid Zn–H<sub>2</sub> hybrid battery by linking the Zn oxidation reaction with the HER as the half-cell reactions occurring in the anode and cathode, respectively. With an OCV of 1.28 V, a power density of 32 mW cm<sup>-2</sup>, and a hydrogen production ability with a Faradaic efficiency of 97%, the proposed hybrid Zn–H<sub>2</sub> battery is found to have the potential to generate H<sub>2</sub> and energy simultaneously. Furthermore, the remarkable ORR activity of the FeHCNR in an acidic medium has been exploited for fabricating an AEZAB by clubbing the Zn oxidation in the anolyte and the ORR in the catholyte. This system provided an OCV of 2.15 V and a power density of 69 mW cm<sup>-2</sup>. In this regard, the hollow structure and enhanced exposure of the active sites of the catalyst presented in this work not only demonstrate the potential to explore a novel bi-functional electrocatalyst, which can ensure simultaneous production of hydrogen and energy, but also point toward feasible opportunities and cost-effective solutions for the designing of more energy-efficient systems for many futuristic applications.

## ASSOCIATED CONTENT

### Supporting Information

The Supporting Information is available free of charge at <https://pubs.acs.org/doi/10.1021/acs.energyfuels.2c01659>.

Material characterizations including experimental sections, digital photographs, FESEM images, SEM images, TEM images, and XPS spectra; electrochemical characterization; and the explanation for electrochemical neutralization energy ([PDF](#))

## AUTHOR INFORMATION

### Corresponding Author

**Sreekumar Kurungot** — *Physical and Materials Chemistry Division, CSIR-National Chemical Laboratory, Pune, Maharashtra 411008, India; Academy of Scientific and Innovative Research (AcSIR), Ghaziabad, Uttar-Pradesh 201002, India; [orcid.org/0000-0001-5446-7923](https://orcid.org/0000-0001-5446-7923); Email: [k.sreekumar@ncl.res.in](mailto:k.sreekumar@ncl.res.in)*

### Authors

**Ajmal Pandikassala** — *Physical and Materials Chemistry Division, CSIR-National Chemical Laboratory, Pune, Maharashtra 411008, India; Academy of Scientific and Innovative Research (AcSIR), Ghaziabad, Uttar-Pradesh 201002, India*

**Pranav K. Gangadharan** — *Physical and Materials Chemistry Division, CSIR-National Chemical Laboratory, Pune, Maharashtra 411008, India; Academy of Scientific and Innovative Research (AcSIR), Ghaziabad, Uttar-Pradesh 201002, India*

**Radhika Nittoor Veedu** — *Physical and Materials Chemistry Division, CSIR-National Chemical Laboratory, Pune, Maharashtra 411008, India*

Complete contact information is available at:  
<https://pubs.acs.org/10.1021/acs.energyfuels.2c01659>

## Author Contributions

All authors have contributed to the paper, and the final version of the manuscript has been approved by the authors.

## Notes

The authors declare no competing financial interest.

## ACKNOWLEDGMENTS

A.P. acknowledges the Council of Scientific and Industrial Research (CSIR), New Delhi, India, for the Research Fellowship. S.K. acknowledges the Department of Science and Technology (DST), New Delhi, for funding through the project GAP328726 (SERB Sanction Order: Sanction Order: CRG/2019/000277).

## ABBREVIATIONS

ORR = oxygen reduction reaction

HER = hydrogen evolution reaction

LSV = linear sweep voltammetry

ADT = accelerated durability test

OCV = open-circuit voltage

AEZAB = asymmetric-electrolyte Zn–air battery

## REFERENCES

- (1) Widera, B. Renewable hydrogen implementations for combined energy storage, transportation and stationary applications. *Therm. Sci. Eng. Prog.* **2020**, *16*, 100460–100468.
- (2) Zhao, G.; Rui, K.; Dou, S. X.; Sun, W. Heterostructures for Electrochemical Hydrogen Evolution Reaction: A Review. *Adv. Funct. Mater.* **2018**, *28*, 1803291–1803317.
- (3) Boyano, A.; Blanco-Marigorta, A. M.; Morosuk, T.; Tsatsaronis, G. Exergoenvironmental analysis of a steam methane reforming process for hydrogen production. *Energy* **2011**, *36*, 2202–2214.
- (4) Jamesh, M.-I.; Kuang, Y.; Sun, X. Constructing Earth-abundant 3D Nanoarrays for Efficient Overall Water Splitting—A Review. *ChemCatChem* **2019**, *11*, 1550–1575.
- (5) Cheddie, D.; Munroe, N. Review and comparison of approaches to proton exchange membrane fuel cell modeling. *J. Power Sources* **2005**, *147*, 72–84.
- (6) Peighambardoust, S. J.; Rowshanzamir, S.; Amjadi, M. Review of the proton exchange membranes for fuel cell applications. *Int. J. Hydrogen Energy* **2010**, *35*, 9349–9384.
- (7) Rosli, R. E.; Sulong, A. B.; Daud, W. R. W.; Zulkifley, M. A.; Husaini, T.; Rosli, M. I.; Majlan, E. H.; Haque, M. A. A review of high-temperature proton exchange membrane fuel cell (HT-PEMFC) system. *Int. J. Hydrogen Energy* **2017**, *42*, 9293–9314.
- (8) Chandan, A.; Hattenberger, M.; El-kharouf, A.; Du, S.; Dhir, A.; Self, V.; Pollet, B. G.; Ingram, A.; Bujalski, W. High temperature (HT) polymer electrolyte membrane fuel cells (PEMFC)—A review. *J. Power Sources* **2013**, *231*, 264–278.
- (9) Guo, Z.; Wang, Y.; Song, Y.; Li, C.; Su, X.; Wang, Y.; Cai, W.-b.; Xia, Y. A Multifunction Lithium–Carbon Battery System Using a Dual Electrolyte. *ACS Energy Lett.* **2017**, *2*, 36–44.
- (10) Cai, P.; Li, Y.; Wang, G.; Wen, Z. Alkaline–Acid Zn–H<sub>2</sub>O Fuel Cell for the Simultaneous Generation of Hydrogen and Electricity. *Angew. Chem., Int. Ed.* **2018**, *57*, 3910–3915.
- (11) Nadeema, A.; Pandurang Kharabe, G.; Prakash Biswal, D.; Kurungot, S. Co@CoAl-Layered Double Hydroxide/Nitrogen-Doped Graphene Composite Catalyst for Al–H<sub>2</sub>O-Based Batteries: Simulta-
- neous Hydrogen Production and Electricity Generation. *ChemElectroChem* **2020**, *7*, 2582–2591.
- (12) Li, H.; Zhang, M.; Yi, L.; Liu, Y.; Chen, K.; Shao, P.; Wen, Z. Ultrafine Ru nanoparticles confined in 3D nitrogen-doped porous carbon nanosheet networks for alkali-acid Zn-H<sub>2</sub> hybrid battery. *Appl. Catal., B* **2021**, *280*, 119412–119420.
- (13) Pu, Z.; Zhao, J.; Amiuu, I. S.; Li, W.; Wang, M.; He, D.; Mu, S. A universal synthesis strategy for P-rich noble metal diphosphide-based electrocatalysts for the hydrogen evolution reaction. *Energy Environ. Sci.* **2019**, *12*, 952–957.
- (14) Bing, Y.; Liu, H.; Zhang, L.; Ghosh, D.; Zhang, J. Nanostructured Pt-alloy electrocatalysts for PEM fuel cell oxygen reduction reaction. *Chem. Soc. Rev.* **2010**, *39*, 2184–2202.
- (15) Shiva Kumar, S.; Himabindu, V. Hydrogen production by PEM water electrolysis—A review. *Mater. Sci. Energy Technol.* **2019**, *2*, 442–454.
- (16) Carmo, M.; Fritz, D. L.; Mergel, J.; Stolten, D. A comprehensive review on PEM water electrolysis. *Int. J. Hydrogen Energy* **2013**, *38*, 4901–4934.
- (17) Zhou, T.; Wang, D.; Chun-Kiat Goh, S.; Hong, J.; Han, J.; Mao, J.; Xu, R. Bio-inspired organic cobalt(II) phosphonates toward water oxidation. *Energy Environ. Sci.* **2015**, *8*, 526–534.
- (18) Zhao, Q.; Hou, M.; Jiang, S.; Wang, S.; Ai, J.; Zheng, L.; Shao, Z. Investigation of a Fe–N–C catalyst for sulfur dioxide electro-oxidation. *RSC Adv.* **2016**, *6*, 80024–80028.
- (19) Stephens, I. E. L.; Chorkendorff, I. Minimizing the Use of Platinum in Hydrogen-Evolving Electrodes. *Angew. Chem., Int. Ed.* **2011**, *50*, 1476–1477.
- (20) Zhang, R.; He, S.; Lu, Y.; Chen, W. Fe, Co, N-functionalized carbon nanotubes in situ grown on 3D porous N-doped carbon foams as a noble metal-free catalyst for oxygen reduction. *J. Mater. Chem. A* **2015**, *3*, 3559–3567.
- (21) Wu, G.; More, K. L.; Johnston, C. M.; Zelenay, P. High-Performance Electrocatalysts for Oxygen Reduction Derived from Polyaniline, Iron, and Cobalt. *Science* **2011**, *332*, 443–447.
- (22) Yang, Z. K.; Lin, L.; Xu, A.-W. 2D Nanoporous Fe–N/C Nanosheets as Highly Efficient Non-Platinum Electrocatalysts for Oxygen Reduction Reaction in Zn-Air Battery. *Small* **2016**, *12*, 5710–5719.
- (23) Choi, H.-J.; Ashok Kumar, N.; Baek, J.-B. Graphene supported non-precious metal-macrocyclic catalysts for oxygen reduction reaction in fuel cells. *Nanoscale* **2015**, *7*, 6991–6998.
- (24) Dou, M.; He, D.; Shao, W.; Liu, H.; Wang, F.; Dai, L. Pyrolysis of Animal Bones with Vitamin B12: A Facile Route to Efficient Transition Metal–Nitrogen–Carbon (TM-N-C) Electrocatalysts for Oxygen Reduction. *Chem.—Eur. J.* **2016**, *22*, 2896–2901.
- (25) Liu, T.; Zhao, P.; Hua, X.; Luo, W.; Chen, S.; Cheng, G. An Fe–N–C hybrid electrocatalyst derived from a bimetal–organic framework for efficient oxygen reduction. *J. Mater. Chem. A* **2016**, *4*, 11357–11364.
- (26) Yasuda, S.; Furuya, A.; Uchibori, Y.; Kim, J.; Murakoshi, K. Iron–Nitrogen-Doped Vertically Aligned Carbon Nanotube Electrocatalyst for the Oxygen Reduction Reaction. *Adv. Funct. Mater.* **2016**, *26*, 738–744.
- (27) Wu, Q.; Yang, L.; Wang, X.; Hu, Z. From Carbon-Based Nanotubes to Nanocages for Advanced Energy Conversion and Storage. *Acc. Chem. Res.* **2017**, *50*, 435–444.
- (28) Yu, L.; Wu, H. B.; Lou, X. W. D. Self-Templated Formation of Hollow Structures for Electrochemical Energy Applications. *Acc. Chem. Res.* **2017**, *50*, 293–301.
- (29) Zhu, Y. P.; Guo, C.; Zheng, Y.; Qiao, S.-Z. Surface and Interface Engineering of Noble-Metal-Free Electrocatalysts for Efficient Energy Conversion Processes. *Acc. Chem. Res.* **2017**, *50*, 915–923.
- (30) Wang, J.; Ciucci, F. Boosting Bifunctional Oxygen Electrolysis for N-Doped Carbon via Bimetal Addition. *Small* **2017**, *13*, 1604103–1604118.
- (31) Wu, Z.-Y.; Xu, S.-L.; Yan, Q.-Q.; Chen, Z.-Q.; Ding, Y.-W.; Li, C.; Liang, H.-W.; Yu, S.-H. Transition metal–assisted carbonization

- of small organic molecules toward functional carbon materials. *Sci. Adv.* **2018**, *4*, No. eaat0788.
- (32) Du, L.; Xing, L.; Zhang, G.; Sun, S. Metal-organic framework derived carbon materials for electrocatalytic oxygen reactions: Recent progress and future perspectives. *Carbon* **2020**, *156*, 77–92.
- (33) Xiang, Q.; Meng, G.; Zhang, Y.; Xu, J.; Xu, P.; Pan, Q.; Yu, W. Ag nanoparticle embedded-ZnO nanorods synthesized via a photochemical method and its gas-sensing properties. *Sens. Actuators, B* **2010**, *143*, 635–640.
- (34) Ai, K.; Liu, Y.; Ruan, C.; Lu, L.; Lu, G. Sp<sup>2</sup>-C-Dominant N-Doped Carbon Sub-micrometer Spheres with a Tunable Size: A Versatile Platform for Highly Efficient Oxygen-Reduction Catalysts. *Adv. Mater.* **2013**, *25*, 998–1003.
- (35) Jiang, W.-J.; Gu, L.; Li, L.; Zhang, Y.; Zhang, X.; Zhang, L.-J.; Wang, J.-Q.; Hu, J.-S.; Wei, Z.; Wan, L.-J. Understanding the High Activity of Fe–N–C Electrocatalysts in Oxygen Reduction: Fe/Fe<sub>3</sub>C Nanoparticles Boost the Activity of Fe–N<sub>x</sub>. *J. Am. Chem. Soc.* **2016**, *138*, 3570–3578.
- (36) Wen, Z.; Ci, S.; Zhang, F.; Feng, X.; Cui, S.; Mao, S.; Luo, S.; He, Z.; Chen, J. Nitrogen-Enriched Core-Shell Structured Fe/Fe<sub>3</sub>C-C Nanorods as Advanced Electrocatalysts for Oxygen Reduction Reaction. *Adv. Mater.* **2012**, *24*, 1399–1404.
- (37) Zhou, H.; Chen, J.; Huang, T.; Chen, D.; Wu, Y.; Zheng, F.; Yu, H.; Li, S. Uniformly distributed and in situ iron–nitrogen codoped porous carbon derived from pork liver for rapid and simultaneous detection of dopamine, uric acid, and paracetamol in human blood serum. *New J. Chem.* **2017**, *41*, 2081–2089.
- (38) Yang, H.; Shang, L.; Zhang, Q.; Shi, R.; Waterhouse, G. I. N.; Gu, L.; Zhang, T. A universal ligand mediated method for large scale synthesis of transition metal single atom catalysts. *Nat. Commun.* **2019**, *10*, 4585.
- (39) Zhou, Y.; Sun, Y.; Wang, H.; Zhu, C.; Gao, J.; Wu, D.; Huang, H.; Liu, Y.; Kang, Z. A nitrogen and boron co-doped metal-free carbon electrocatalyst for an efficient oxygen reduction reaction. *Inorg. Chem. Front.* **2018**, *5*, 2985–2991.
- (40) Zhou, X.; Bai, Z.; Wu, M.; Qiao, J.; Chen, Z. 3-Dimensional porous N-doped graphene foam as a non-precious catalyst for the oxygen reduction reaction. *J. Mater. Chem. A* **2015**, *3*, 3343–3350.
- (41) Sa, Y. J.; Seo, D.-J.; Woo, J.; Lim, J. T.; Cheon, J. Y.; Yang, S. Y.; Lee, J. M.; Kang, D.; Shin, T. J.; Shin, H. S.; Jeong, H. Y.; Kim, C. S.; Kim, M. G.; Kim, T.-Y.; Joo, S. H. A General Approach to Preferential Formation of Active Fe–N<sub>x</sub> Sites in Fe–N/C Electrocatalysts for Efficient Oxygen Reduction Reaction. *J. Am. Chem. Soc.* **2016**, *138*, 15046–15056.
- (42) Li, C.; Lv, Y.; Guo, L.; Xu, H.; Ai, X.; Zhang, J. Raman and excitonic photoluminescence characterizations of ZnO star-shaped nanocrystals. *J. Lumin.* **2007**, *122*–123, 415–417.
- (43) Russo, V.; Ghidelli, M.; Gondoni, P.; Casari, C. S.; Li Bassi, A. L. Multi-wavelength Raman scattering of nanostructured Al-doped zinc oxide. *J. Appl. Phys.* **2014**, *115*, 073508–073518.
- (44) Dong, Z. W.; Zhang, C. F.; Deng, H.; You, G. J.; Qian, S. X. Raman spectra of single micrometer-sized tubular ZnO. *Mater. Chem. Phys.* **2006**, *99*, 160–163.
- (45) Wang, X.; Zhang, P.; Wang, W.; Lei, X.; Zou, B.; Yang, H. Synthesis, structure and magnetic properties of graphite carbon encapsulated Fe<sub>3</sub>C nanoparticles for applications as adsorbents. *RSC Adv.* **2015**, *5*, 27857–27861.
- (46) Wang, X.; Zhang, P.; Gao, J.; Chen, X.; Yang, H. Facile synthesis and magnetic properties of Fe<sub>3</sub>C/C nanoparticles via a sol–gel process. *Dyes Pigm.* **2015**, *112*, 305–310.
- (47) Maldonado, S.; Stevenson, K. J. Direct Preparation of Carbon Nanofiber Electrodes via Pyrolysis of Iron(II) Phthalocyanine: Electrocatalytic Aspects for Oxygen Reduction. *J. Phys. Chem. B* **2004**, *108*, 11375–11383.
- (48) Tang, Y.; Allen, B. L.; Kauffman, D. R.; Star, A. Electrocatalytic Activity of Nitrogen-Doped Carbon Nanotube Cups. *J. Am. Chem. Soc.* **2009**, *131*, 13200–13201.
- (49) Yan, J.; Meng, H.; Xie, F.; Yuan, X.; Yu, W.; Lin, W.; Ouyang, W.; Yuan, D. Metal free nitrogen doped hollow mesoporous graphene-analogous spheres as effective electrocatalyst for oxygen reduction reaction. *J. Power Sources* **2014**, *245*, 772–778.
- (50) Liu, H.; Li, Y.; Yuan, M.; Sun, G.; Liao, Q.; Zhang, Y. Solid and macroporous Fe<sub>3</sub>C/N-C nanofibers with enhanced electromagnetic wave absorability. *Sci. Rep.* **2018**, *8*, 16832–16844.
- (51) Joshi, B.; Lee, J.-G.; Samuel, E.; Jo, H. S.; Kim, T.-G.; Swihart, M. T.; Yoon, W. Y.; Yoon, S. S. Supersonically blown reduced graphene oxide loaded Fe–Fe<sub>3</sub>C nanofibers for lithium ion battery anodes. *J. Alloys Compd.* **2017**, *726*, 114–120.
- (52) Zhang, H.; Gong, Q.; Ren, S.; Arshid, M. A.; Chu, W.; Chen, C. Implication of iron nitride species to enhance the catalytic activity and stability of carbon nanotubes supported Fe catalysts for carbon-free hydrogen production via low-temperature ammonia decomposition. *Catal. Sci. Technol.* **2018**, *8*, 907–915.
- (53) Zhou, D.; Yang, L.; Yu, L.; Kong, J.; Yao, X.; Liu, W.; Xu, Z.; Lu, X. Fe/N/C hollow nanospheres by Fe(III)-dopamine complexation-assisted one-pot doping as nonprecious-metal electrocatalysts for oxygen reduction. *Nanoscale* **2015**, *7*, 1501–1509.
- (54) Jiang, H.; Yao, Y.; Zhu, Y.; Liu, Y.; Su, Y.; Yang, X.; Li, C. Iron Carbide Nanoparticles Encapsulated in Mesoporous Fe–N-Doped Graphene-Like Carbon Hybrids as Efficient Bifunctional Oxygen Electrocatalysts. *ACS Appl. Mater. Interfaces* **2015**, *7*, 21511–21520.
- (55) Tang, F.; Lei, H.; Wang, S.; Wang, H.; Jin, Z. A novel Fe–N–C catalyst for efficient oxygen reduction reaction based on polydopamine nanotubes. *Nanoscale* **2017**, *9*, 17364–17370.
- (56) Lin, L.; Zhu, Q.; Xu, A.-W. Noble-Metal-Free Fe–N/C Catalyst for Highly Efficient Oxygen Reduction Reaction under Both Alkaline and Acidic Conditions. *J. Am. Chem. Soc.* **2014**, *136*, 11027–11033.
- (57) Fujimoto, A.; Yamada, Y.; Koinuma, M.; Sato, S. Origins of sp<sup>3</sup>C peaks in C1s X-ray Photoelectron Spectra of Carbon Materials. *Anal. Chem.* **2016**, *88*, 6110–6114.
- (58) Wang, Z.; Dong, Y.; Li, H.; Zhao, Z.; Bin Wu, H.; Hao, C.; Liu, S.; Qiu, J.; Lou, X. W. Enhancing lithium–sulphur battery performance by strongly binding the discharge products on amino-functionalized reduced graphene oxide. *Nat. Commun.* **2014**, *5*, 5002–5010.
- (59) Lai, L.; Potts, J. R.; Zhan, D.; Wang, L.; Poh, C. K.; Tang, C.; Gong, H.; Shen, Z.; Lin, J.; Ruoff, R. S. Exploration of the active center structure of nitrogen-doped graphene-based catalysts for oxygen reduction reaction. *Energy Environ. Sci.* **2012**, *5*, 7936–7942.
- (60) Li, J.; Zhang, H.; Samarakoon, W.; Shan, W.; Cullen, D. A.; Karakalos, S.; Chen, M.; Gu, D.; More, K. L.; Wang, G.; Feng, Z.; Wang, Z.; Wu, G. Thermally Driven Structure and Performance Evolution of Atomically Dispersed FeN<sub>4</sub> Sites for Oxygen Reduction. *Angew. Chem., Int. Ed.* **2019**, *58*, 18971–18980.
- (61) Zhu, C.; Shi, Q.; Xu, B. Z.; Fu, S.; Wan, G.; Yang, C.; Yao, S.; Song, J.; Zhou, H.; Du, D.; Beckman, S. P.; Su, D.; Lin, Y. Hierarchically Porous M–N–C (M = Co and Fe) Single-Atom Electrocatalysts with Robust MN<sub>x</sub> Active Moieties Enable Enhanced ORR Performance. *Adv. Energy Mater.* **2018**, *8*, 1801956.
- (62) Zhang, J.; He, D.; Su, H.; Chen, X.; Pan, M.; Mu, S. Porous polyaniline-derived FeNx/C/C catalysts with high activity and stability towards oxygen reduction reaction using ferric chloride both as an oxidant and iron source. *J. Mater. Chem. A* **2014**, *2*, 1242–1246.
- (63) Qiao, Z.; Hwang, S.; Li, X.; Wang, C.; Samarakoon, W.; Karakalos, S.; Li, D.; Chen, M.; He, Y.; Wang, M.; Liu, Z.; Wang, G.; Zhou, H.; Feng, Z.; Su, D.; Spendelow, J. S.; Wu, G. 3D porous graphitic nanocarbon for enhancing the performance and durability of Pt catalysts: a balance between graphitization and hierarchical porosity. *Energy Environ. Sci.* **2019**, *12*, 2830–2841.
- (64) Ao, X.; Zhang, W.; Li, Z.; Li, J.-G.; Soule, L.; Huang, X.; Chiang, W.-H.; Chen, H. M.; Wang, C.; Liu, M.; Zeng, X. C. Markedly Enhanced Oxygen Reduction Activity of Single-Atom Fe Catalysts via Integration with Fe Nanoclusters. *ACS Nano* **2019**, *13*, 11853–11862.
- (65) Mao, Y.; Duan, H.; Xu, B.; Zhang, L.; Hu, Y.; Zhao, C.; Wang, Z.; Chen, L.; Yang, Y. Lithium storage in nitrogen-rich mesoporous carbon materials. *Energy Environ. Sci.* **2012**, *5*, 7950–7955.

- (66) Xue, J.; Li, Y.; Hu, J. Nanoporous bimetallic Zn/Fe–N–C for efficient oxygen reduction in acidic and alkaline media. *J. Mater. Chem. A* **2020**, *8*, 7145–7157.
- (67) Wu, Z.-Y.; Xu, X.-X.; Hu, B.-C.; Liang, H.-W.; Lin, Y.; Chen, L.-F.; Yu, S.-H. Iron Carbide Nanoparticles Encapsulated in Mesoporous Fe-N-Doped Carbon Nanofibers for Efficient Electrocatalysis. *Angew. Chem., Int. Ed.* **2015**, *54*, 8179–8183.
- (68) Liang, H.-W.; Wei, W.; Wu, Z.-S.; Feng, X.; Müllen, K. Mesoporous Metal–Nitrogen-Doped Carbon Electrocatalysts for Highly Efficient Oxygen Reduction Reaction. *J. Am. Chem. Soc.* **2013**, *135*, 16002–16005.
- (69) Wu, G.; Johnston, C. M.; Mack, N. H.; Artyushkova, K.; Ferrandon, M.; Nelson, M.; Lezama-Pacheco, J. S.; Conradson, S. D.; More, K. L.; Myers, D. J.; Zelenay, P. Synthesis–structure–performance correlation for polyaniline–Me–C non-precious metal cathode catalysts for oxygen reduction in fuel cells. *J. Mater. Chem.* **2011**, *21*, 11392–11405.
- (70) Gangadharan, P. K.; Pandikassala, A.; Kurungot, S. Toward pH Independent Oxygen Reduction Reaction by Polydopamine Derived 3D Interconnected, Iron Carbide Embedded Graphitic Carbon. *ACS Appl. Mater. Interfaces* **2021**, *13*, 8147–8158.
- (71) Wu, G.; Chung, H. T.; Nelson, M.; Artyushkova, K.; More, K. L.; Johnston, C. M.; Zelenay, P. Graphene-Riched  $\text{Co}_9\text{S}_8$ -N-C Non-Precious Metal Catalyst for Oxygen Reduction in Alkaline Media. *ECS Trans.* **2011**, *41*, 1709–1717.
- (72) Lin, Z.; Song, M.-k.; Ding, Y.; Liu, Y.; Liu, M.; Wong, C.-p. Facile preparation of nitrogen-doped graphene as a metal-free catalyst for oxygen reduction reaction. *Phys. Chem. Chem. Phys.* **2012**, *14*, 3381–3387.
- (73) Jeon, I.-Y.; Yu, D.; Bae, S.-Y.; Choi, H.-J.; Chang, D. W.; Dai, L.; Baek, J.-B. Formation of Large-Area Nitrogen-Doped Graphene Film Prepared from Simple Solution Casting of Edge-Selectively Functionalized Graphite and Its Electrocatalytic Activity. *Chem. Mater.* **2011**, *23*, 3987–3992.
- (74) Yang, W.; Liu, X.; Yue, X.; Jia, J.; Guo, S. Bamboo-like Carbon Nanotube/Fe<sub>3</sub>C Nanoparticle Hybrids and Their Highly Efficient Catalysis for Oxygen Reduction. *J. Am. Chem. Soc.* **2015**, *137*, 1436–1439.
- (75) Luo, Z.; Lim, S.; Tian, Z.; Shang, J.; Lai, L.; MacDonald, B.; Fu, C.; Shen, Z.; Yu, T.; Lin, J. Pyridinic N doped graphene: synthesis, electronic structure, and electrocatalytic property. *J. Mater. Chem.* **2011**, *21*, 8038–8044.
- (76) Masa, J.; Xia, W.; Muhler, M.; Schuhmann, W. On the Role of Metals in Nitrogen-Doped Carbon Electrocatalysts for Oxygen Reduction. *Angew. Chem., Int. Ed.* **2015**, *54*, 10102–10120.
- (77) Mahmood, N.; Yao, Y.; Zhang, J.-W.; Pan, L.; Zhang, X.; Zou, J.-J. Electrocatalysts for Hydrogen Evolution in Alkaline Electrolytes: Mechanisms, Challenges, and Prospective Solutions. *Adv. Sci.* **2018**, *5*, 1700464–1700487.
- (78) Zuo, Q.; Zhao, P.; Luo, W.; Cheng, G. Hierarchically porous Fe–N–C derived from covalent-organic materials as a highly efficient electrocatalyst for oxygen reduction. *Nanoscale* **2016**, *8*, 14271–14277.
- (79) Alves, V. A.; da Silva, L. A.; Boodts, J. F. C. Surface characterisation of IrO<sub>2</sub>/TiO<sub>2</sub>/CeO<sub>2</sub> oxide electrodes and Faradaic impedance investigation of the oxygen evolution reaction from alkaline solution. *Electrochim. Acta* **1998**, *44*, 1525–1534.
- (80) McCrory, C. C. L.; Jung, S.; Peters, J. C.; Jaramillo, T. F. Benchmarking Heterogeneous Electrocatalysts for the Oxygen Evolution Reaction. *J. Am. Chem. Soc.* **2013**, *135*, 16977–16987.
- (81) Wu, G.; Nelson, M. A.; Mack, N. H.; Ma, S.; Sekhar, P.; Garzon, F. H.; Zelenay, P. Titanium dioxide-supported non-precious metal oxygen reduction electrocatalyst. *Chem. Commun.* **2010**, *46*, 7489–7491.
- (82) Gao, W.; Havas, D.; Gupta, S.; Pan, Q.; He, N.; Zhang, H.; Wang, H.-L.; Wu, G. Is reduced graphene oxide favorable for nonprecious metal oxygen-reduction catalysts? *Carbon* **2016**, *102*, 346–356.
- (83) Poulin, S.; França, R.; Moreau-Bélanger, L.; Sacher, E. Confirmation of X-ray Photoelectron Spectroscopy Peak Attributions of Nanoparticulate Iron Oxides, Using Symmetric Peak Component Line Shapes. *J. Phys. Chem. C* **2010**, *114*, 10711–10718.
- (84) Singh, S. K.; Kashyap, V.; Manna, N.; Bhange, S. N.; Soni, R.; Boukherroub, R.; Szunerits, S.; Kurungot, S. Efficient and Durable Oxygen Reduction Electrocatalyst Based on CoMn Alloy Oxide Nanoparticles Supported Over N-Doped Porous Graphene. *ACS Catal.* **2017**, *7*, 6700–6710.
- (85) Cai, P.; Li, Y.; Chen, J.; Jia, J.; Wang, G.; Wen, Z. An Asymmetric-Electrolyte Zn–Air Battery with Ultrahigh Power Density and Energy Density. *ChemElectroChem* **2018**, *5*, 589–592.
- (86) Ramp, F. L. Secondary batteries powered by forced ionisation. *Nature* **1979**, *278*, 335–337.
- (87) Vermaas, D. A.; Smith, W. A. Synergistic Electrochemical CO<sub>2</sub> Reduction and Water Oxidation with a Bipolar Membrane. *ACS Energy Lett.* **2016**, *1*, 1143–1148.
- (88) Luo, J.; Vermaas, D. A.; Bi, D.; Hagfeldt, A.; Smith, W. A.; Grätzel, M. Bipolar Membrane-Assisted Solar Water Splitting in Optimal pH. *Adv. Energy Mater.* **2016**, *6*, 1600100.